CANDELS: Correlations of SEDs and Morphologies with Star-formation Status for Massive Galaxies at $z \sim 2$

Tao Wang[1,2], Jia-Sheng Huang[2], S. M. Faber[3], Guanwen Fang[4,2], Stijn Wuyts[5], G. G. Fazio[2], Haojing Yan[6], Avishai Dekel[7], Yicheng Guo[8], Henry C. Ferguson[9], Norman Grogin[9], Jennifer M. Lotz[9], Benjamin Weiner[10], Elizabeth J. McGrath[3], Dale Kocevski[3], Nimish P. Hathi[11], Ray A. Lucas[9], A.M.Koekemoer[9], Xu Kong[4], and Qiu-Sheng Gu[1]

taowang@nju.edu.cn

ABSTRACT

We present a study on Spectral Energy Distributions, Morphologies, and star formation for an IRAC-selected extremely red object sample in the GOODS Chandra Deep Field-South. This work was enabled by new *HST*/WFC3 near-IR imaging from the CANDELS survey as well as the deepest available X-ray data from *Chandra* 4 Ms observations. This sample consists of 133 objects with the 3.6μm limiting magnitude of [3.6] = 21.5, and is approximately complete for galaxies with $M_* > 10^{11} M_\odot$ at $1.5 \leq z \leq 2.5$. We classify this sample into two types, quiescent and star-forming galaxies, in the observed infrared color-color ([3.6]–[24] vs K–[3.6]) diagram. The further morphological study of this sample show a consistent result with the observed color classification. The classified quiescent galaxies are bulge dominated and star-forming galaxies in the sample have disk or irregular morphologies. Our observed infrared

[1]School of Astronomy & Space Science, Nanjing University, Nanjing 210093, China

[2]Harvard-Smithsonian Center for Astrophysics, 60 Garden Street, Cambridge, MA 02138, USA

[3]University of California Observatories/Lick Observatory, University of California, Santa Cruz, CA 95064, USA

[4]Center for Astrophysics, University of Science and Technology of China, Hefei 230026, China

[5]Max-Planck-Institut für Extraterrestrische Physik, Giessenbachstrasse, 85748 Garching, Germany

[6]Department of Physics and Astronomy, University of Missouri, Columbia, MO 65211, USA

[7]Racah Institute of Physics, The Hebrew University, Jerusalem 91904, Israel

[8]Astronomy Department, University of Massachusetts, 710 N. Pleasant Street, Amherst, MA 01003, USA

[9]Space Telescope Science Institute, 3700 San Martin Dr., Baltimore, MD 21218, USA

[10]Steward Observatory, University of Arizona, 933 North Cherry Avenue, Tucson, AZ 85721, USA

[11]Carnegie Observatories, 813 Santa Barbara Street, Pasadena, CA 91101, USA

color classification is also consistent with the rest-frame color (U−V vs V−J) classification. We also found that quiescent and star-forming galaxies are well separated in the nonparametric morphology parameter (Gini vs M_{20}) diagram measuring their concentration and clumpiness: quiescent galaxies have Gini coefficient higher than 0.58 and star forming galaxies have Gini coefficient lower that 0.58. We argue that the star formation quenching process must lead to or be accompanied by the increasing galaxy concentration. One prominent morphological feature of this sample is that disks are commonly seen in this massive galaxy sample at $1.5 \leq z \leq 2.5$: 30% of quiescent galaxies and 70% of star forming galaxies with $M_* > 10^{11} M_\odot$ have disks in their rest-frame optical morphologies. The prevalence of these extended, relatively undisturbed disks challenges the merging scenario as the main mode of massive galaxy formation.

Subject headings: galaxies: evolution — galaxies: formation — galaxies: high-redshift — galaxies: structure

1. Introduction

Understanding when and how the most massive galaxies formed remains one of the most outstanding problems in galaxy formation. In the present-day universe, most massive galaxies ($M \gtrsim 10^{11} M_\odot$) are early-type galaxies (Baldry et al. 2004), which are primarily composed of old stellar populations with no or little star formation. Spectroscopic studies of large local samples reveal that the bulk of stellar mass in massive early-type galaxies was formed at $z \gtrsim 1.5$ within a short timescale (Thomas et al. 2005; Renzini 2006; Jimenez et al. 2007, and refs. therein). At intermediate redshifts, several surveys reveal that the precursors of present-day massive early-type galaxies have already turned passive by $z \sim 0.8$, but may continue to assemble their stellar mass later through dry mergers (Bell et al. 2004; Yamada et al. 2005; Bundy et al. 2006; Cimatti et al. 2006; Borch et al. 2006; Faber et al. 2007; Brown et al. 2007). The lack of significant star formation in these galaxies since $z = 0.8$ implies that their stellar mass formed at higher redshifts. Recently, both observational and theoretical results suggest that the critical epoch for massive galaxy evolution and mass assembly is at $1 \lesssim z \lesssim 3$ (Fontana et al. 2004; Glazebrook et al. 2004; Nagamine et al. 2005; Kong et al. 2006; Papovich et al. 2006; Abraham et al. 2007; Arnouts et al. 2007; Ilbert et al. 2010). Thus, a complete census of a well-defined massive galaxy sample at this redshift range is crucial to understanding the formation and evolution of these objects.

Significant progress has been made in detecting and identifying massive galaxies at $1 \lesssim z \lesssim 3$ using large-format near-infrared (NIR) array cameras on 4–10 m class telescopes. Recent wide-field NIR surveys reveal several "new" galaxy populations, which includes Extremely Red Objects

(EROs; $R-K>5$, Elston et al. 1988), IRAC-selected EROs ($z_{850}-[3.6]>3.25$[1], Yan et al. 2004), BzKs (sBzK:$(z-K)-(B-z)>-0.2$, pBzK: $z-K>2.5$; Daddi et al. 2004), and Distant Red Galaxies (DRGs, $J-K>2.3$, Franx et al. 2003). These galaxy populations are mainly selected on the basis of their red rest-frame optical colors, and have typical stellar masses in excess of $10^{11}M_{\odot}$ down to current NIR limits. Moreover, various studies show that they dominate the high-mass regime of the $z\sim2$ stellar mass function (SMF). For instance, Conselice et al. (2008) suggested that EROs contribute 75% of all $M_{*}>10^{11}M_{\odot}$ galaxies at $z\sim1.5$ down to K_{Vega} = 19.7, while van Dokkum et al. (2006) found a similar fraction for DRGs in the range of $2<z<3$. This makes red color selection an efficient and effective way of studying massive high-redshift galaxies.

Utilizing these novel techniques for identifying high-redshift massive galaxies, a great deal of work has been carried out to explore their nature. These galaxies turn to be very different from their local counterparts. First, star formation activities were more intense at higher redshifts. At $z\sim2$, more than half of the massive galaxies are rapidly star-forming galaxies with $\gtrsim100M_{\odot}\mathrm{yr}^{-1}$ while the remaining are quiescent galaxies with no or little ongoing star-formation (Papovich et al. 2006; Daddi et al. 2007; Cassata et al. 2008; Kriek et al. 2008). In contrast, at $z\sim0$ most of the galaxies with similar mass are quiescent galaxies. Second, while the cosmic mass density in massive star-forming galaxies is flat or decreases from $z\sim2$ to the present day, the mass density in massive quiescent galaxies increases by a factor of ~10 over the same time period. Such dramatic evolution can not be fully explained by modest mass growth of individual quiescent galaxies. Transformation of the star-forming galaxies into quiescent galaxies is indispensable to match this density evolution of quiescent galaxies, as well as that of star-forming galaxies themselves (see, e.g., Brammer et al. 2011). Understanding this transformation is now one of the central questions in studying galaxy evolution.

To study the physical mechanisms responsible for this transformation, it is essential to classify galaxies into different types. Though a clear bimodal color distribution between quiescent and star-forming galaxies persists to at least $z\approx1$, the bimodality becomes less distinct at the high-mass end (e.g., Strateva et al. 2001; Blanton et al. 2003; Baldry et al. 2004; Bell et al. 2004; Faber et al. 2007). This may be largely attributed to an increase in dust content in the massive star-forming galaxies which reddens their colors (Baldry et al. 2004, 2006; Driver et al. 2007). The dust reddening turns to be more significant at higher redshifts due to increasing importance of obscured star-formation. At $z\sim2$ most massive star-forming galaxies have very red optical-to-infrared colors. Indeed, these star-forming galaxies have such red colors that they are prematurely on the red sequence (Brammer et al. 2009). A number of other methods were proposed to separate the two populations, using for example, observed colors $I-J$ vs. $J-K$ (Pozzetti & Mannucci

[1] z_{850} is the F850LP band magnitude.

2000), rest-frame colors $U-V$ vs. $V-J$ (Wuyts et al. 2007; Williams et al. 2009), mid-infrared colors (Papovich et al. 2006; Fontana et al. 2009), or directly using output spectral types and specific star-formation rates (SSFR[2]) from the SED fitting process (Arnouts et al. 2007; Damen et al. 2009; Ilbert et al. 2010; Guo et al. 2011). Each of these techniques has its advantages and disadvantages, and they can give different classification results for a significant number of galaxies. Resolving these discrepancies is important for us to have a clean separation of quiescent and star-forming populations. Moreover, the fraction of AGNs among massive galaxies at $z \sim 2$ is high, up to $\sim$ 30% (see, e.g., Messias et al. 2010). AGN activity can also contribute to the infrared emission, which is used to identify star-forming galaxies in most of the classification methods. Thus a comprehensive identification of AGN population is necessary for a better understanding of galaxy classification.

In addition to the star-formation status, morphologies provide important constrains on the galaxy assembly history and are crucial to distinguish among models of galaxy formation (Roberts & Haynes 1994). Studies of morphologies for high-redshift galaxies have greatly advanced in the last decade (Papovich et al. 2005; Lotz et al. 2006; Toft et al. 2007; Buitrago et al. 2008; Cameron et al. 2011; Förster Schreiber et al. 2011; Kartaltepe et al. 2011). Several recent work present evidence that galaxy morphologies are correlated with star-forming status for galaxies at $z \sim 2$: quiescent galaxies tend to be spheroidal and compact while star-forming galaxies are mostly disks or irregular/mergers with larger sizes (Daddi et al. 2005; Toft et al. 2007; van Dokkum et al. 2008; Buitrago et al. 2008; Kriek et al. 2009a; Damjanov et al. 2009; Szomoru et al. 2010; Cassata et al. 2011; Weinzirl et al. 2011; Wuyts et al. 2011; Bell et al. 2011). However, this correlation at $z \sim 2$ shows large scatter and is far from clear. A significant number of systems are classified as having the same star-formation status yet with different morphological types (see, e.g., Conselice et al. 2011a). Based on the new *HST*/WFC3 NIR imaging, van der Wel et al. (2011) shows that $\sim$ 65% of quiescent galaxies are actually disk-dominated (also see, Cameron et al. 2011), though their sample is small . Moreover, many of these work characterized galaxy structures with the Sérsic index obtained by fitting a Sérsic model to the surface brightness data, i.e., a model-dependent approach. Yet there are concerns whether the profile of a high-redshift galaxy can be well fitted with a single sérsic profile (Szomoru et al. 2010). Thus other methods, including both visual classification and model-independent measurement of galaxy morphology, are needed to probe the relationship between galaxy morphology and their physical properties. Nevertheless, this requires high-resolution and high signal-to-nosie NIR (rest-frame optical) imaging for a statistical sample of $z \sim 2$ galaxies, which now becomes available thanks to the Cosmic Assembly Near-infrared Deep Extragalactic Legacy Survey (CANDELS; PI: Sandra M. Faber and Henry C. Ferguson, cf, Grogin et al. 2011; Koekemoer et al. 2011).

[2] SFR per stellar mass, SSFR = SFR/M_*

In this paper, we present a study on star-formation activity, morphologies, and rest-frame colors for a sample of massive galaxies at $z \sim 2$ selected in the GOODS-South. This work was enabled by the new *HST*/WFC3 near-IR imaging from the CANDELS as well as the deepest available X-ray data from *Chandra* 4 Ms observations. These new data, supplemented with the available rich data set in this field, allows us to have a better separation between quiescent galaxies, star-forming galaxies, and AGNs. We use a sample of bright IRAC-selected Extremely Red Objects (Yan et al. 2004), which effectively reject low-redshift contaminates. Conselice et al. (2011b) argue that the IERO selection is the most efficient among other methods (EROs, *BzK*s, and DRGs) for identifying massive galaxy samples at $1.5 < z < 3$.

The structure of this paper is as follows. The sample selection is described in section 2. We discuss the classification between quiescent and star-forming galaxies based on their star-formation status in section 3. Both visual classification and nonparametric approaches are performed on their *HST*/WFC3 F160W morphologies in section 4. After separating quiescent and star-forming galaxies, we derive their redshift and stellar mass in section 5. We examine the joint distribution of star formation activity, morphology and rest-frame colors in section 6. A summary of our main results is given in section 7. Throughout the paper, we assume $\Omega_\Lambda = 0.7$, $\Omega_M = 0.3$, and $H_0 = 70$ km s^{-1} Mpc^{-1}. All magnitudes are in the AB system unless specified otherwise, and the notation "[3.6]" means the AB magnitude at wavelength 3.6 μm.

2. Data Sets and IERO Selection

The GOODS Chandra Deep Field-South (GOODS-S, Giavalisco et al. 2004) is among the best studied deep fields, with a rich multi-wavelength data set. The ultradeep IRAC imaging of GOODS-S covers the whole $10' \times 15'$ region (Dickinson et al., in preparation) and has an exposure time of 23 hrs per pointing, yielding a 5σ limiting magnitude of [3.6] $\sim$ 25.6. Zheng et al. (2012, in preparation) reprocessed all GTO and legacy IRAC survey data in five CANDELS fields including the GOODS-S to produce a homogeneous catalogue. We adopted their 3.6 μm selected sample as our primary catalogue.

Giavalisco et al. (2004) performed very deep ACS imaging including F435W, F606W, F775W, and F850LP bands in the GOODS-S, with a 5σ limiting magnitude of $z_{850} \sim 27.3$. Retzlaff et al. (2010) also carried out deep VLT/ISAAC NIR imaging in this field, with limiting magnitudes J = 25.0, H = 24.5, and K_s = 24.4 (5σ). The deep NIR photometry is essential for deriving accurate photometric redshifts and stellar masses for red galaxies at $z \sim 2$ (Wuyts et al. 2007).

MIPS 24 μm (Rieke et al. 2004) is very sensitive to dust emission from galaxies in the redshift range $0 < z < 3$ (Huang et al. 2005, 2009; Yan et al. 2005; Webb et al. 2006; Papovich et al. 2007),

and is thus extremely useful to identify the dusty star-forming population in red galaxies. The 24 μm imaging in the GOODS-S is the deepest ever obtained with an exposure time of 10 hour per pointing. The 3σ point-source sensitivity limit is $\sim 10\mu$Jy, permitting detection of luminous infrared galaxies (LIRGs) with $L_{IR} \sim 2 \times 10^{11} L_{\odot}$ out to $z \sim 2.5$. On the other hand, the 24 μm emission from a galaxy can also be powered by an AGN, which can be identified by deep X-ray observations. The recent 4 Ms *Chandra* imaging in the GOODS-S, the deepest *Chandra* survey ever obtained, reaches on-axis flux limits of $\approx 3.2 \times 10^{-17}$, 9.1×10^{-18}, and 5.5×10^{-17} erg cm^{-2} s^{-1} for the full (0.5−8 keV), soft (0.5−2 keV), and hard bands (2−8 keV), respectively (Xue et al. 2011). These deep X-ray data permit detection of even highly obscured AGNs.

A major breakthrough in deep imaging of GOODS-S comes from two recent *HST*/WFC3 NIR surveys: the WFC3 Early Release Science (ERS, Windhorst et al. 2011) program and the first phase of the CANDELS survey. The ERS mosaic covers the northern $10' \times 4'$ region of GOODS-S while the CANDELS dataset covers the southern $10' \times 12'$ region. Both surveys reach 5σ limiting magnitude of $\gtrsim 27.0$ in F160W (H-band), providing high-quality structural information (concentrations, Gini/M$_{20}$) for galaxies as faint as $H = 24.6$, which is equivalent to $2 \times 10^{10} M_{\odot}$ at $z \sim 2$ (Grogin et al. 2011).

The sample is selected within the central 138 arcmin^2 area in the GOODS-S where deep ACS, WFC3, ISAAC, and IRAC data are all available. We set criteria

$$[z_{850}] - [3.6] > 3.25 \qquad \textit{and} \qquad [3.6] < 21.5 \tag{1}$$

to select a bright IERO sample. Figure 1 shows that the color criterion $[z_{850}] - [3.6] > 3.25$ mainly selects quiescent galaxies and dusty star-forming galaxies at $z \gtrsim 1$ (Yan 2008). Their red colors are due to either the Balmer/4000 Å break shifting beyond F850LP or their steep slope of the rest-frame UV spectra. Young and blue galaxies can not reach this threshold even at higher redshifts. Thus simple $z_{850} - [3.6]$ cut are very effective in selecting galaxy samples at high-redshift. Moreover, the bright magnitude cut of $[3.6] < 21.5$ ensures that all galaxies in this sample have high-quality SEDs as well as reliable morphological measurements. Our final IERO sample includes 133 galaxies. The median z_{850} band magnitude in our sample is $z_{850} \sim 24.6$, and 80% of them have at least a 3σ detection in all the ACS and IRAC bands. For comparison, the IERO sample in Yan et al. (2004) is much fainter with a median $z_{850} \sim 27$. We then matched these sources to the FIREWORKS catalog (Wuyts et al. 2008) and obtained multi-wavelength photometry from ground-based U band to *Spitzer*/MIPS 24 μm. 29% of the sample, or 38 sources, have an X-ray counterpart in the 4 Ms *Chandra* source catalog within a search radius of 1.5″.

Figure 1 also shows the distribution of their [3.6] – [4.5] colors for this sample, which can be used to constrain their redshifts. Most galaxies in the sample have [3.6] – [4.5] > 0, indicating that they are mainly at $z \gtrsim 1.5$ when the 1.6 μm stellar emission bump begins to move into the

IRAC 4.5 μm band (Sawicki 2002; Huang et al. 2004; Papovich 2008; Huang et al. 2009). Their photometric redshifts are presented in section 5.

3. Separating IEROs into Quiescent and Star-forming Populations based on [3.6] – [24] color

We have shown that the IEROs tend to be either quiescent galaxies (quiescents) or dusty star-forming galaxies (dSFGs) at $z > 1.5$. However, it is difficult to separate them solely based on observed UV-to-NIR SEDs. Instead, the mid-infrared, e.g., the MIPS 24 μm, traces star-forming activity across a wide range of redshifts, and can be used to separate these two populations (Papovich et al. 2006; Fontana et al. 2009; Fang et al. 2009). In particular, in redshift $1.5 < z < 2.5$ the 7.7 μm PAH emission shifts into the observed 24 μm, allowing a universal conversion of 24 μm flux into star-formation rate (SFR,Papovich et al. 2007; Rieke et al. 2009; Elbaz et al. 2011). On the other hand, the IRAC 3.6 μm in this redshift range probes rest-frame NIR, which can be treated as a good proxy for stellar mass (Bell & de Jong 2001; Cole et al. 2001). Thus we argue that the [3.6] – [24] color provides a good indicator of specific star-formation rates (SSFR) for galaxies in this sample.

We plot K – [3.6] vs. [3.6] – [24] color-color diagram for X-ray undetected and X-ray detected IEROs in Figure 2a and Figure 2b, respectively. The IEROs show a clearly bimodal distribution in the [3.6] – [24] color. The 3σ limiting flux density at 24 μm in the GOODS-S is $\sim 11\mu$Jy, equivalent to a SFR of $\sim 10\ M_{\odot}$ yr^{-1} at $z \sim 2$ (Rieke et al. 2009). IEROs have a typical stellar mass of $\sim 10^{11} M_{\odot}$ (see,e.g, Yan et al. 2004), thus this 24 μm detection limit is equivalent to a SSFR $\sim 10^{-10}$ yr^{-1}. All the 24 μm-undetected galaxies are in the $[3.6]-[24] < 0.3$ region in Figure 2, and we propose an empirical color criterion, [3.6] – [24] = 0.3, to classify this sample into quiescents and dSFGs. This criterion is consistent with that used in Damen et al. (2009)[3] We also verified that by changing the [3.6] – [24] color criterion within a scatter of 0.2, the numbers in the quiescents and dSFGs population changed at most ∼10%, and our main conclusions drawn in this paper remain valid.

In several cases, 24 μm emission may be very weak or absent even for dSFGs. At $z \sim 1.4$, the silicate absorption at 9.7μm shifts in the MIPS 24 μm band. Thus SFGs with a strong silicate absorption feature may have no 24 μm detection at this redshift (Magdis et al. 2011). We thus propose another K – [3.6] color to At $z \sim 2$, K – [3.6] probes rest-frame $R-J$, which is sensitive to

[3]Damen et al. (2009) adopted $SSFR < 1/(3 \times t_H)$ yr^{-1} to select quiescents, where t_H is the age of the universe at a given redshift. This criterion is used to characterize the low-SSFR peak of massive galaxies, which increases with redshift. At $z = 2$ this yields $SSFR \lesssim 10^{-10}$ yr^{-1}.

dust extinction. DSFGs have redder K – [3.6] colors compared to quiescents at similar redshifts, as shown by the color tracks of a quiescent and a dSFG SED template in Figure 2a. Most objects in our sample with $[3.6]-[24] < 0.3$ have blue K – [3.6] , but a few of them have very red K – [3.6] (see galaxies to left of dashed line in Figure 2(a)). Photometric redshifts for these sources confirm that they are at $z \sim 1.4$ or at very high redshift, $z \sim 3$, where 24μm is not sensitive to star formation. We argue that these sources are really dSFGs. We therefore propose the observable color criteria for identification of quiescents in the sample as:

$$[3.6]-[24] < 0.3 \ \ and \ \ K-[3.6] < 1.2. \tag{2}$$

The remaining objects are denoted as dSFGs. We note that though the adopted $K-[3.6]$ color criterion is empirical, the number of these 24 μm–faint dSFGs is very small and have redshifts beyond our main interests.

Based on Eq 2, a total of 90 galaxies, 68% of the whole sample, are classified as dSFGs; 43 galaxies, 32% of the whole sample, are quiescents. The median [3.6] – [24] colors for the two populations are $\sim$ 2.2 and –0.5, respectively, indicating that their SSFRs are significantly different. In fact, those galaxies with [3.6] – [24] $>$ 0.3 have a median 24 μm flux density of $\sim$ 125 μJy, implying that a significant fraction of them are ultra-luminous infrared galaxies (ULIRGs) at $z \sim 2$. Roughly 30% of this IERO sample, 38 sources, are detected at X-ray, all of which are classified as AGNs according to their X-ray luminosities in Xue et al. (2011). Among these X-ray IEROs, 79% are dSFGs and the remaining 21% are quiescents. We do note that quiescent galaxies with AGNs, which can also have strong 24 μm emission (see, e.g., Gu et al. 2007), may be misidentified as dSFGs. As shown in Figure 2b, several AGNs even show very blue K – [3.6] contrary to their red [3.6] – [24]. Further classification of these X-ray IEROs will be performed using their morphologies and rest-frame colors.

4. Morphologies of IEROs from *HST*/WFC3 NIR Imaging

Galaxy morphologies provide additional information on the mass assembly history of galaxies (Bell et al. 2005; Zheng et al. 2004). We performed both visual classifications and nonparametric morphological measurements to see whether quiescents and dSFGs in our sample can be separated based on their morphologies. All morphological analysis in this work are based on the CANDELS 6-epoch v2.0 drizzled mosaics for the WFC3 F160W band, with a pixel scale of 0.06″,

4.1. Visual Classification

The IEROs in our sample show very diversified morphologies, covering a wide range of types from extended and disturbed low surface brightness features to bulge-dominated morphology. We divide morphological types for this sample into three broad categories:

Spheroid: Single, round, and centrally concentrated source with no evidence of extended low surface brightness features.

Disk: Undisturbed source with extended low surface brightness features.

Irregular/Merger: Single highly irregular galaxy with evidence of non-axisymmetric, extended low surface-brightness features or two or more distinct galaxies showing distortions and interaction features such as tidal arms.

Figure 3 shows typical examples of the three types in the WFC3 F160W images. Visual inspections for this sample were performed by three of the co-authors independently. We combined the classifications from each inspector and reviewed the sources together to resolve the disagreements, which involved $\sim$ 15% of the sample. The final visual morphological types are listed in Table 1. About 40% of this sample are classified as disk galaxies, 30% are spheroids and the remaining 30% are irregular/mergers. The X-ray sources have the similar fractions of disk, spheroid and irregular/merger types: 45%, 20% and 35% respectively. Most of the X-ray sources show a bulge component even they are identified as disk galaxies (see also, Kocevski et al. 2011).

We present F160W images for quiescents and dSFGs in Figures 4 and 5, respectively. Roughly 70% of the quiescent galaxies are spheroids, and 30% of them show a significant disk component. The dSFGs, in contrast, are either regular disks or irregular/mergers, with only a few being spheroids. It should be noted that he quiescent disks are significantly different from the star-forming disks: the former also have a prominent bulge while the latter have small or no bulges. Thus we can separate the two populations based on whether they have a significant bulge component: Both spheroids and those disks with a prominent bulge are quiescents while the remaining galaxies are dSFGs.

4.2. Nonparametric Morphological Parameters

Nonparametric morphological parameters, such as Gini and M_{20}, have now become popular in the automated identification of galaxy morphology. These parameters do not rely on certain model parameter fits, such as the Sérsic index, and therefore can be applied to irregulars as well as standard Hubble-type galaxies (Lotz et al. 2004). The Gini coefficient is a concentration parameter, measuring the relative distribution of the galaxy pixel flux values. It is high for galaxies with much

of their light concentrated in a small number of pixels, regardless whether those pixels are in the projected center. Therefore, the Gini method has the advantage that it do not require the galaxy to be circularly symmetric, and is particularly useful for galaxies at high redshifts, which can have very distorted morphologies. M_{20} describes the second-order moment of the brightest 20% of the galaxy's flux, which is very sensitive to merger signatures such as multiple nuclei, tidal tails, and off-center star clusters. Gini and M_{20} are shown to be closely related with visual morphologies for galaxies both at low and intermediate redshifts: early-type galaxies have higher Gini and lower M_{20} while late-type galaxies have lower Gini and higher M_{20} (Lotz et al. 2006; Abraham et al. 2007; Capak et al. 2007; Lotz et al. 2008; Kong et al. 2009). At higher redshift, however, it is difficult to measure Gini and M_{20} due to a lack of high-quality NIR (rest-frame optical) images. And their relationships with visual morphologies, as well as star-forming status remain unclear. The new WFC3 data from CANDELS provides NIR imaging with sufficient angular resolution and depth, allowing us to reliably measure Gini and M_{20} for a representative sample of massive galaxies at $z \sim 2$.

We calculated Gini and M_{20} for galaxies in our sample using the WFC3 F160W images following the definition of

$$G = \frac{\sum_i^N (2i - N - 1)|f_i|}{(N-1)\sum_i^N |f_i|} \tag{3}$$

where N is the number of pixels within the images and f_i are the fluxes for each pixel sorted in ascending order with $|f_1| \leq |f_2| \leq ... \leq |f_N|$, and

$$M_{20} \equiv \log 10 \left(\frac{\sum_j M_j}{M_{tot}} \right) \quad \text{while} \quad \sum_j f_j < 0.2 \sum_j^N |f_j| \tag{4}$$

$$M_{tot} = \sum_j^N M_j = \sum_j^N f_j \cdot ((x_j - x_c)^2 + (y_j - y_c)^2) \tag{5}$$

(Lotz et al. 2004; Abraham et al. 2007) ,where x_c, y_c is the galaxy's center and f_j are the fluxes for each pixel sorted in descending order with $|f_1| \geq |f_2| \geq ... \geq |f_N|$ (Lotz et al. 2004; Abraham et al. 2007). Details of our procedure can be found in Abraham et al. (2007). We shows the distribution of Gini and M_{20} for our sample in Figure 6, with randomly selected measurements marked by their stamp images.

Galaxies of different visual morphological types occupy different regions in the Gini-M_{20} diagram (Figures 6 and 7). Spheroids have higher Gini and lower M_{20}, while most irr/mergers have lower Gini and high M_{20}. The disks span a wide range in both Gini and M_{20}: those disks with a prominent bulge tend to have higher Gini and lower M_{20} whereas disks with small or no bulges have lower Gini and higher M_{20}.

For the non-X-ray IEROs, quiescents and dSFGs are well separated in the Gini-M_{20} diagram: nearly all quiescents have Gini > 0.58, while dSFGs have Gini < 0.58 with only a few outliers. To further verify this, we re-plot Figure 2 but now with each object color-coded according to the Gini coefficient, as shown in Figure 8. This diagram shows that the IR color criteria used in Eq 2 to select quiescents also succeeded in choosing objects with Gini $\gtrsim 0.58$. The three sources with [3.6] – [24] < 0.3 and red K – [3.6] > 1.2 have very low Gini coefficient, suggesting that they are not quiescents.

X-ray IEROs are plotted in Figure 8(b). They show inconsistent classification between their IR colors and quantitive morphological parameters. While most of the X-ray sources in the quiescent region of Figure 2 show higher Gini [4], nine X-ray sources have Gini > 0.58 yet have [3.6] – [24] > 0.3, placing them outside the quiescent region. There are two possible reasons for these sources to cross the line: they are quiescents with strong bulges and their 24 μm emission is from central AGNs, or they are dSFGs with powerful AGNs appearing in their H-band images and causing an increase in Gini. We do notice that, however, most of these sources show a significant bulge except one source with ID 1325 appearing to be a point source (Figure 5). In fact, among all the X-ray sources in our sample, 66% (25 sources) of them have $L_X < 5 \times 10^{43}$ erg s^{-1} while only 15% (6 sources) have $L_X > 1 \times 10^{44}$ erg s^{-1} (Xue et al. 2011). Thus we argue that contamination from the AGN in optical bands is not significant for most X-ray sources. Those with high gini are likely caused by a significant bulge component. We will further verify this with their rest-frame colors in Section 6.

Though the adopted technique has been used and tested by many previous works (see, e.g., Abraham et al. 2007; Capak et al. 2007; Kong et al. 2009), we evaluate the accuracy and reliability of Gini and M_{20} in the following ways. We have already shown that there is good correspondence between visual morphological types and their distribution in the $Gini - M_{20}$ diagram (Figures 6 and 7). Thus the $Gini - M_{20}$ system provides a reliable way to automatically distinguish different morphological types of galaxies in our sample. Many previous works show that below a certain S/N level $<$ S/N $>\sim 2$, Gini and M_{20} depend on the S/N ratio and is useless for distinguishing different populations (Lotz et al. 2004; Lisker 2008). Benefiting from the bright cut, the median magnitude in the F160W band is $H \sim 22.5$. And all their images have a mean S/N per pixel $<$ S/N $>> 2$ with a median of $< S/N >\sim 10$ (Lotz et al. 2012, in preparation). Therefore, the *Gini* and M_{20} for our sample do not suffer S/N effect. As an independent check, we also calculated galaxy central concentration, the concentration index (C, Abraham et al. 1994), using also F160W images and compared it with *Gini* (Figure 9). Our calculated C is closely correlated with *Gini*, consistent with that shown in previous works (Abraham et al. 2003). This confirms that galaxies

[4]The only one that shows very low Gini coefficient, ID 1404, is a high-z source, as discussed in Figure 4.

with high *Gini* indeed are more concentrated. The $Gini-C$ relation shows larger scatter for objects with low concentration, mostly dSFGs. This is also expected: measurements of C is based on simple aperture photometry, under the assumption that galaxies are circularly symmetric and have a well-defined center; however, neither of these assumptions can be fulfilled for the dSFGs in this sample. Thus we conclude that our calculated *Gini* and M_{20} provides reliable measurement of galaxy concentration and clumpiness for galaxies in our sample.

5. Photometric Redshifts and Stellar Masses

5.1. Photometric Redshifts

Only $\sim$ 23%, 31 galaxies, of the IEROs in our sample have spectroscopic redshifts (z_{spec}), and therefore we derive photometric redshifts (z_{ph}) for the rest using the standard SED fitting technique. After separating our IEROs into quiescents and dSFGs, we are able to select SEDs accordingly to do SED fitting.

We used the single stellar population (SSP) models of Bruzual & Charlot (2003, hereafter BC03) to construct a template set for the quiescents. We assumed solar metallicity and Calzetti extinction law (Calzetti et al. 2000) in the range of $0 \leq A_V \leq 0.5$ mag. For the 10 quiescents with spectroscopic redshifts, we obtain very good agreement between z_{ph} and z_{spec}, with the normalized median absolute deviation σ_{NMAD}[5] = 0.03. Figure 10 shows that the SEDs of the quiescent IEROs in our sample are well fit by these SSP models, with best-fit ages ranging from 0.4 Gyr to 4 Gyr. Many of them also show a rest-frame UV excess, which is likely due to an additional young stellar population component (see also Yan et al. 2004). However, the UV excess does not affect the resulting photometric redshifts, which are mainly determined by the rest-frame optical-to-MIR SEDs.

The dSFGs are much more diverse in that they span a wide range in their [3.6]−[24] colors and show a large variety of morphological characteristics. We fit these dusty galaxies using the "Easy and Accurate Zphot from Yale" (EAzY; Brammer et al. 2008). We allow for a linear combination of six templates which can recover the entire rest-frame color space occupied by observed galaxies. An accuracy of σ_{NMAD} = 0.07 was obtained for the 19 dSFGs with spectroscopic redshifts, and their SEDs are shown in Figure 11.

[5]Defined as 1.48 $\times$ median($|z_{spec}-z_{ph}|/(1+z_{spec})$) (Brammer et al. 2008)

5.2. Stellar Masses

To obtain stellar masses, we fit the observed B-to-4.5 μm SEDs of both the quiescent and dSFGs using "Fitting and Assessment of Synthetic Templates" (FAST; Kriek et al. 2009b). We fixed their redshifts at the derived redshift, and fit the SEDs to a set of simple stellar population models. These models have exponentially declining star-formation histories (SFH) with $0.1 < \tau < 10$ Gyr and $0 \leq A_V \leq 4$ assuming Calzetti law. We adopted a Salpeter (Salpeter 1955) initial mass function and solar metallicity. The stellar masses derived from the best-fitting template are then scaled to a Kroupa IMF (Kroupa 2001) by dividing the Salpeter stellar mass by a factor of 1.6 (Marchesini et al. 2009). We have verified that by using the Maraston (2005) model instead of BC03 models, the stellar mass is systematically smaller with an offset of –0.20 and a scatter of 0.17. This is consistent with previous studies for $z \sim 2$ samples (Muzzin et al. 2009; Marchesini et al. 2009). We also compared our stellar mass estimates with that derived using the approach in Wuyts et al. (2007, 2008), which fitted three different star formation histories: a single stellar population (SSP) without dust, a constant star formation (CSF) history with dust (A_v varying from 0 to 4), and an exponentially declining star formation history with an e-folding timescale of 300 Myr and the same range of A_v. The two methods give fairly consistent results with a offset of –0.02 and a scatter of 0.13.

The mass and redshift distributions are shown in Figure 12. We also derive the mass completeness limit as a function of redshift for a 3.6 μm selected ($[3.6] < 21.5$) sample. This completeness limit is calculated using the full and deeper FIREWORKS catalog following the method in Marchesini et al. (2009). While these IEROs span a wide range of $1 \leq z_{ph} \leq 4$, most of them are in $1.5 < z < 2.5$ within a narrow peak centered at $z_{ph} = 1.8$. Their derived stellar masses are more striking, with a median value of $\sim 1 \times 10^{11} M_{\odot}$. All this is in broad agreement with the prototype IERO sample of Yan et al. (2004). These IEROs are clearly among the most massive galaxies. At $M > 10^{11} M_{\odot}$ (where the our sample is nearly complete; see below), the fraction of quiescents increases significantly from $\sim 22\%$ at $2 \leq z \leq 2.5$ to $\sim 43\%$ at $1.5 \leq z \leq 2$ (Table 1), suggesting that we are seeing the quenching process in action in the most massive systems (also see, e.g., Cameron et al. 2011).

It is important to understand the completeness of this sample in terms of stellar mass. For this purpose, we compare our work to that of FIREWORKS (Wuyts et al. 2008), where the K-band selected sample is complete at $M \geq 10^{10.5} M_{\odot}$ to $z \sim 3$. The mass completeness of a flux-limited sample is clearly a function of redshift, and here we concentrate on the redshift range of $1.5 \leq z \leq 2.5$ because this is where we are most interested. As stated above, the approach for deriving stellar mass for the FIREWORKS galaxies gives consistent results as our estimates. We find that our IERO sample has recovered $\sim 80\%$ of the FIREWORKS galaxies at $M \geq 10^{11} M_{\odot}$ within $1.5 \leq z \leq 2.5$, as shown in Figure 13.

The other 20% (nine galaxies) have $z_{850}-[3.6] < 3.25$ mag and thus are missed by our selection. Among these nine galaxies, four of them are X-ray sources (Luo et al. 2008; Xue et al. 2011), and they also have the highest MIPS 24 μm fluxes. The SEDs of these four objects have strong AGN components, which may have caused their stellar masses to be overestimated. The other five galaxies have just slightly bluer $z_{850}-[3.6]$ colors than the IERO criterion, and only one is not detected in MIPS 24 μm. They are clearly at the border of being selected as IEROs. We hence argue that the IERO selection using $z_{850}-[3.6] > 3.25$ mag and $[3.6] < 21.5$ mag is nearly complete at $M_* \geq 10^{11} M_\odot$ at $1.5 \leq z \leq 2.5$ except for the bluest galaxies.

6. Rest-frame Properties of IEROs

The rest-frame colors permit additional characterization of galaxies. Wuyts et al. (2007) and Williams et al. (2009) proposed that quiescents and dSFGs can be separated in rest-frame $U-V$ versus $V-J$: while both quiescents and dSFGs show red $U-V$ colors either due to old stellar populations or dust extinction, quiescents are bluer in $V-J$ due to lack of dust reddening. We computed these two colors by interpolating observed data following the algorithm of Rudnick et al. (2003), as shown in Figure 14. The rest-frame colors uncertainties were calculated using the input photometry through Monte Carlo simulations. For each galaxy, we created mock SEDs using a Gaussian distribution and calculated their rest-frame *UVJ* colors. This procedure was repeated 1000 times to derive the uncertainties for their color estimation. The average 1σ error ellipse is shown in the lower left of Figure 14a.

Quiescents and dSFGs in the sample can be well separated in the *UVJ* diagram (Figure 14a), consistent with our classification based on the observed IR colors and morphological parameters. However, there are a few quiescents lying just across the dividing line which may be due to either photometric errors or that they suffering extinctions. While we can locate these galaxies in the quiescent region by pushing the dividing line to redder $V-J$ colors, many dSFGs will also enter the quiescent region. In fact, we verified that the observed $K-[3.6]$ colors for these outliers are also redder than other quiescent galaxies at similar redshifts. Interestingly, most of these outliers show edge-on disk morphologies in their F160w images, e.g., ID 1127, ID 2614, and ID 6292 (Figure 4), indicating that they suffer more severe dust extinction. X-ray sources can also be separated in the *UVJ* diagram (Figure 14b): those X-ray sources with high *Gini* are in the quiescent regions, despite that several of them are classified as dSFGs based on the IR colors. We argue that these X-ray sources with high *Gini* may have significant bulges, yet their 24 μm mainly comes from AGN.

Quiescents and dSFGs can not be separated in the color-mass diagram (CMD) as shown in Figure 15 and Figure 16. We confine our analysis on their distribution in the CMD to the non-X-ray

IEROs in $1.5 < z < 2.5$, where our sample is nearly complete for the most massive galaxies. The dashed red line is the red sequence criterion at z = 2 extrapolated from the same criterion at z < 1 in Borch et al. (2006). Both quiescents and dSFGs in this sample are massive and red. Particularly, Figure 15 shows that the $U-V$ colors span a wide range for quiescents. It is also interesting to note that the distribution of spheroids and disks appears similar in the CMD. These quiescent disks contribute $\sim 30\%$ of the whole quiescent population in $1.5 < z < 2.5$, confirming pervious findings (van der Wel et al. 2011; Cameron et al. 2011; Kartaltepe et al. 2011). For the dSFGs, we find that disk galaxies tend to be more massive and have redder $U-V$ than the Irr/Mergers (Figure 16). In fact, as shown in Table 1, 70% of the massive dSFGs are disks. These disks are very extended and do not show clear signatures of mergers/interactions from visual inspection. M_{20} for most of these disks is smaller than that for Irr/Mergers (Figure 6), suggesting that they are relatively undisturbed. These properties are incompatible with the expected compact or highly perturbed morphologies of ongoing mergers. Instead, the stochastic accretion of gas may play a greater role in the formation of massive disks (Förster Schreiber et al. 2006; Dekel et al. 2009; Martig et al. 2009; Genzel et al. 2006, 2011; Förster Schreiber et al. 2011).

7. Conclusions

With the new *Chandra* 4 Ms imaging and *HST*/WFC3 F160W imaging from CANDELS, we studied relationships between SEDs, morphologies, and star-formation status for a sample of 133 IRAC-selected Extremely Red Objects (IEROs) with $z_{850}-[3.6] > 3.25$ mag and $[3.6] < 21.5$ mag in the GOODS-S. These criteria select high-mass galaxies at $z \gtrsim 1.5$, and our sample is nearly mass-complete at $M_* > 10^{11} M_\odot$ within $1.5 \leq z \leq 2.5$. The IEROs show a clear bimodality in their IR colors, and we find that they can be classified into quiescent galaxies and dusty star-forming galaxies according to their star-formation activities. Such a classification produces very consistent results with that using *Gini* and rest-frame colors ($U-V$ vs. $V-J$), which indicates that these quantities are closely related. Roughly 67% of IEROs in this sample are dusty star-forming galaxies while the remaining 33% are quiescent galaxies. At $M > 10^{11} M_\odot$, the fraction of quiescents increases significantly from $\sim 22\%$ at $2 \leq z \leq 2.5$ to $\sim 43\%$ at $1.5 \leq z \leq 2$. Among the whole IERO sample $\sim 30\%$, or 38 sources, are AGNs, and the identification of these AGNs are shown to be very important in understanding the discrepancies among different classification methods. A number of galaxies are identified as star-forming galaxies based on their 24 μm emission, yet are in the quiescent region of the *UVJ* diagram; we show that most of them are actually AGNs.

The morphological study in this work provides important clues to massive galaxy evolution at $z \sim 2$. The quiescent and dSFGs in this sample show distinctive morphologies. While all quiescents have a prominent bulge, most of the dSFGs are either disks or irregular/mergers with no or

small bulges. This suggests that a prominent bulge is necessary to form a massive quiescent galaxy. We also show that the two populations can be well separated based on the Gini coefficient. The quiescents have higher Gini coefficients than the dSFGs, indicating that the formers are more concentrated. We argue that the quenching process for star formation must lead to or is accompanied by the increase of galaxy concentration.

Roughly 30% of the quiescents also show an extended disk component, confirming recent findings with a larger sample. Moreover, we also find that $\sim 70\%$ of massive dSFGs with $M_* > 10^{11} M_\odot$ at $1.5 \leq z \leq 2.5$ are classified as disk galaxies. Most of these disks appear relatively undisturbed with no clear signatures of mergers/interactions, based on both visual inspection and quantitative measurements. The prevalence of disks among massive galaxies at $z \sim 2$ challenges the merging scenario as the main mode of massive galaxy formation, and suggests that the stochastic accretion of gas plays a greater role.

This work is based on observations taken by the CANDELS Multi-Cycle Treasury Program with the NASA/ESA HST, which is operated by the Association of Universities for Research in Astronomy, Inc., under NASA contract NAS5-26555. We gratefully acknowledge R. Abraham for access to his morphology analysis code. This work is also supported under the National Natural Science Foundation of China under grants (10878010, 10221001, 10873012 and 10633040) and the National Basic Research Program (973 programe no. 2007CB815404 and 2007CB815405).

REFERENCES

Abraham, R. G., Valdes, F., Yee, H. K. C., & van den Bergh, S. 1994, ApJ, 432, 75

Abraham, R. G., van den Bergh, S., & Nair, P. 2003, ApJ, 588, 218

Abraham, R. G., et al. 2007, ApJ, 669, 184

Arnouts, S., et al. 2007, A&A, 476, 137

Baldry, I. K., Balogh, M. L., Bower, R. G., Glazebrook, K., Nichol, R. C., Bamford, S. P., & Budavari, T. 2006, MNRAS, 373, 469

Baldry, I. K., Glazebrook, K., Brinkmann, J., Ivezić, Ž., Lupton, R. H., Nichol, R. C., & Szalay, A. S. 2004, ApJ, 600, 681

Bell, E. F., & de Jong, R. S. 2001, ApJ, 550, 212

Bell, E. F., et al. 2004, ApJ, 608, 752

—. 2005, ApJ, 625, 23

—. 2011, arXiv:1110.3786

Blanton, M. R., et al. 2003, ApJ, 594, 186

Borch, A., et al. 2006, A&A, 453, 869

Brammer, G. B., van Dokkum, P. G., & Coppi, P. 2008, ApJ, 686, 1503

Brammer, G. B., et al. 2009, ApJ, 706, L173

—. 2011, ApJ, 739, 24

Brown, M. J. I., Dey, A., Jannuzi, B. T., Brand, K., Benson, A. J., Brodwin, M., Croton, D. J., & Eisenhardt, P. R. 2007, ApJ, 654, 858

Bruzual, G., & Charlot, S. 2003, MNRAS, 344, 1000

Buitrago, F., Trujillo, I., Conselice, C. J., Bouwens, R. J., Dickinson, M., & Yan, H. 2008, ApJ, 687, L61

Bundy, K., et al. 2006, ApJ, 651, 120

Calzetti, D., Armus, L., Bohlin, R. C., Kinney, A. L., Koornneef, J., & Storchi-Bergmann, T. 2000, ApJ, 533, 682

Cameron, E., Carollo, C. M., Oesch, P. A., Bouwens, R. J., Illingworth, G. D., Trenti, M., Labbé, I., & Magee, D. 2011, ApJ, 743, 146

Capak, P., Abraham, R. G., Ellis, R. S., Mobasher, B., Scoville, N., Sheth, K., & Koekemoer, A. 2007, ApJS, 172, 284

Cassata, P., et al. 2008, A&A, 483, L39

—. 2011, ApJ, 743, 96

Cimatti, A., Daddi, E., & Renzini, A. 2006, A&A, 453, L29

Cole, S., et al. 2001, MNRAS, 326, 255

Coleman, G. D., Wu, C., & Weedman, D. W. 1980, ApJS, 43, 393

Conselice, C. J., Bluck, A. F. L., Ravindranath, S., Mortlock, A., Koekemoer, A. M., Buitrago, F., Grützbauch, R., & Penny, S. J. 2011a, MNRAS, 417, 2770

Conselice, C. J., Bundy, K., U, V., Eisenhardt, P., Lotz, J., & Newman, J. 2008, MNRAS, 383, 1366

Conselice, C. J., et al. 2011b, MNRAS, 413, 80

Daddi, E., Cimatti, A., Renzini, A., Fontana, A., Mignoli, M., Pozzetti, L., Tozzi, P., & Zamorani, G. 2004, ApJ, 617, 746

Daddi, E., et al. 2005, ApJ, 626, 680

—. 2007, ApJ, 670, 156

Damen, M., Labbé, I., Franx, M., van Dokkum, P. G., Taylor, E. N., & Gawiser, E. J. 2009, ApJ, 690, 937

Damjanov, I., et al. 2009, ApJ, 695, 101

Dekel, A., Sari, R., & Ceverino, D. 2009, ApJ, 703, 785

Dey, A., Graham, J. R., Ivison, R. J., Smail, I., Wright, G. S., & Liu, M. C. 1999, ApJ, 519, 610

Driver, S. P., Popescu, C. C., Tuffs, R. J., Liske, J., Graham, A. W., Allen, P. D., & de Propris, R. 2007, MNRAS, 379, 1022

Elbaz, D., et al. 2011, A&A, 533, A119

Elston, R., Rieke, G. H., & Rieke, M. J. 1988, ApJ, 331, L77

Faber, S. M., et al. 2007, ApJ, 665, 265

Fang, G.-W., Kong, X., & Wang, M. 2009, Research in Astronomy and Astrophysics, 9, 59

Fontana, A., et al. 2004, A&A, 424, 23

—. 2009, A&A, 501, 15

Förster Schreiber, N. M., et al. 2006, ApJ, 645, 1062

—. 2011, ApJ, 739, 45

Franx, M., et al. 2003, ApJ, 587, L79

Genzel, R., et al. 2006, Nature, 442, 786

—. 2011, ApJ, 733, 101

Giavalisco, M., et al. 2004, ApJ, 600, L93

Glazebrook, K., et al. 2004, Nature, 430, 181

Grogin, N. A., et al. 2011, ApJS, 197, 35

Gu, Q.-S., Huang, J.-S., Wilson, G., & Fazio, G. G. 2007, ApJ, 671, L105

Guo, Y., et al. 2011, ApJ, 735, 18

Huang, J.-S., et al. 2004, ApJS, 154, 44

—. 2005, ApJ, 634, 137

—. 2009, ApJ, 700, 183

Ilbert, O., et al. 2010, ApJ, 709, 644

Jimenez, R., Bernardi, M., Haiman, Z., Panter, B., & Heavens, A. F. 2007, ApJ, 669, 947

Kartaltepe, J. S., et al. 2011, arXiv:1110.4057

Kocevski, D. D., et al. 2011, ArXiv e-prints

Koekemoer, A. M., et al. 2011, ApJS, 197, 36

Kong, X., Fang, G., Arimoto, N., & Wang, M. 2009, ApJ, 702, 1458

Kong, X., et al. 2006, ApJ, 638, 72

Kriek, M., van Dokkum, P. G., Franx, M., Illingworth, G. D., & Magee, D. K. 2009a, ApJ, 705, L71

Kriek, M., van Dokkum, P. G., Labbé, I., Franx, M., Illingworth, G. D., Marchesini, D., & Quadri, R. F. 2009b, ApJ, 700, 221

Kriek, M., et al. 2008, ApJ, 677, 219

Kroupa, P. 2001, MNRAS, 322, 231

Lisker, T. 2008, ApJS, 179, 319

Lotz, J. M., Madau, P., Giavalisco, M., Primack, J., & Ferguson, H. C. 2006, ApJ, 636, 592

Lotz, J. M., Primack, J., & Madau, P. 2004, AJ, 128, 163

Lotz, J. M., et al. 2008, ApJ, 672, 177

Luo, B., et al. 2008, ApJS, 179, 19

Magdis, G. E., et al. 2011, A&A, 534, A15

Maraston, C. 2005, MNRAS, 362, 799

Marchesini, D., van Dokkum, P. G., Förster Schreiber, N. M., Franx, M., Labbé, I., & Wuyts, S. 2009, ApJ, 701, 1765

Martig, M., Bournaud, F., Teyssier, R., & Dekel, A. 2009, ApJ, 707, 250

Messias, H., Afonso, J., Hopkins, A., Mobasher, B., Dominici, T., & Alexander, D. M. 2010, ApJ, 719, 790

Muzzin, A., Marchesini, D., van Dokkum, P. G., Labbé, I., Kriek, M., & Franx, M. 2009, ApJ, 701, 1839

Nagamine, K., Cen, R., Hernquist, L., Ostriker, J. P., & Springel, V. 2005, ApJ, 627, 608

Papovich, C. 2008, ApJ, 676, 206

Papovich, C., Dickinson, M., Giavalisco, M., Conselice, C. J., & Ferguson, H. C. 2005, ApJ, 631, 101

Papovich, C., et al. 2006, ApJ, 640, 92

—. 2007, ApJ, 668, 45

Pozzetti, L., & Mannucci, F. 2000, MNRAS, 317, L17

Renzini, A. 2006, ARA&A, 44, 141

Retzlaff, J., Rosati, P., Dickinson, M., Vandame, B., Rité, C., Nonino, M., Cesarsky, C., & GOODS Team. 2010, A&A, 511, 50

Rieke, G. H., Alonso-Herrero, A., Weiner, B. J., Pérez-González, P. G., Blaylock, M., Donley, J. L., & Marcillac, D. 2009, ApJ, 692, 556

Rieke, G. H., et al. 2004, ApJS, 154, 25

Roberts, M. S., & Haynes, M. P. 1994, ARA&A, 32, 115

Rudnick, G., et al. 2003, ApJ, 599, 847

Salpeter, E. E. 1955, ApJ, 121, 161

Sawicki, M. 2002, AJ, 124, 3050

Stern, D., Chary, R., Eisenhardt, P. R. M., & Moustakas, L. A. 2006, AJ, 132, 1405

Strateva, I., et al. 2001, AJ, 122, 1861

Szomoru, D., et al. 2010, ApJ, 714, L244

Thomas, D., Maraston, C., Bender, R., & Mendes de Oliveira, C. 2005, ApJ, 621, 673

Toft, S., et al. 2007, ApJ, 671, 285

van der Wel, A., et al. 2011, ApJ, 730, 38

van Dokkum, P. G., et al. 2006, ApJ, 638, L59

—. 2008, ApJ, 677, L5

Webb, T. M. A., et al. 2006, ApJ, 636, L17

Weinzirl, T., et al. 2011, ApJ, 743, 87

Williams, R. J., Quadri, R. F., Franx, M., van Dokkum, P., & Labbé, I. 2009, ApJ, 691, 1879

Windhorst, R. A., et al. 2011, ApJS, 193, 27

Wuyts, S., Labbé, I., Schreiber, N. M. F., Franx, M., Rudnick, G., Brammer, G. B., & van Dokkum, P. G. 2008, ApJ, 682, 985

Wuyts, S., et al. 2007, ApJ, 655, 51

—. 2011, ApJ, 742, 96

Xue, Y. Q., et al. 2011, ApJS, 195, 10

Yamada, T., et al. 2005, ApJ, 634, 861

Yan, H. 2008, in American Institute of Physics Conference Series, Vol. 966, Relativistic Astrophysics, ed. C. L. Bianco & S.-S. Xue, 71–76

Yan, H., et al. 2004, ApJ, 616, 63

Yan, L., et al. 2005, ApJ, 628, 604

Zheng, X. Z., Hammer, F., Flores, H., Assémat, F., & Pelat, D. 2004, A&A, 421, 847

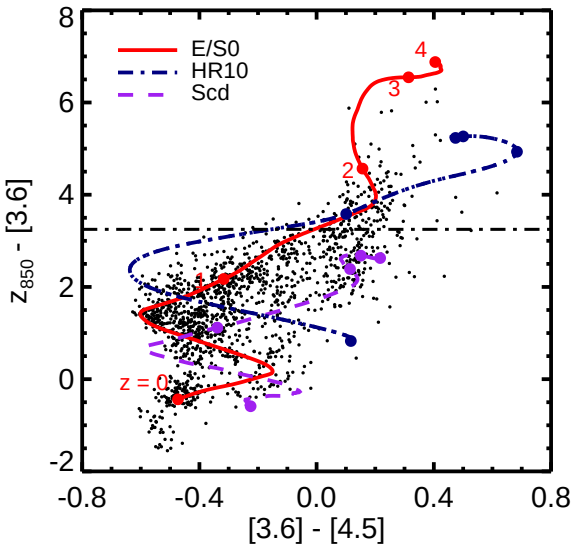

Fig. 1.— Observed-frame z_{850} – [3.6] vs. [3.6] – [4.5] color-color diagram for all IRAC-selected ([3.6] < 21.5) galaxies in the GOODS-S. Observed-frame color tracks for nonevolving E/S0, Scd SEDs (CWW E, Coleman et al. 1980), and a dusty star-forming galaxy (HR10, Dey et al. 1999; Stern et al. 2006) SED at $0 < z < 4$ are plotted using color-coded lines. The IERO color definition, $z_{850}-[3.6] > 3.25$, is marked with a black dashed line. The red $z_{850}-[3.6]$ color can be produced by both old and dusty galaxies at $z \gtrsim 1$.

Table 1. Visual classification results for IEROs in our sample.

Type	All	Spheroids	Disks	Irr/Mergers
Total	133 (38) [a]	34 (8)	59 (17)	40 (13)
Quiescents	43 (8)	25 (2)	15 (4)	3 (2)
dSFGs	90 (30)	9 (6)	44 (13)	37 (11)
Massive [b] Quiescents at $1.5 \leq z < 2.0$	10 (6)	4 (2)	5 (3)	1 (1)
Massive Quiescents at $2.0 \leq z < 2.5$	4 (0)	2	1	1
Massive dSFGs at $1.5 \leq z < 2.0$	13 (5)	1 (1)	8 (3)	4 (1)
Massive dSFGs at $2.0 \leq z < 2.5$	14	0	11	3 (1)

[a]The number of X-ray sources.

[b]$M_* > 10^{11} M_\odot$, where our sample is nearly complete.

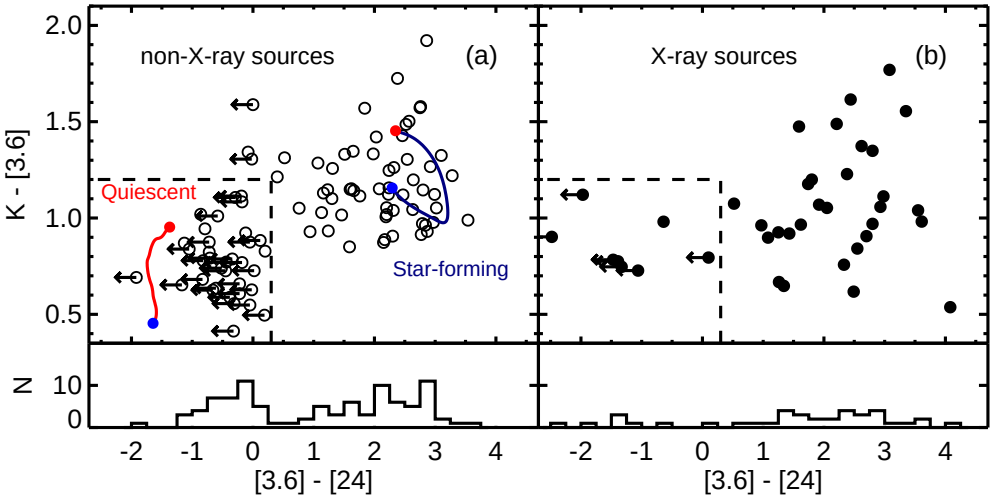

Fig. 2.— The [3.6] – [24] vs $K-[3.6]$ color-color diagram for galaxies in our sample, which is divided into non-X-ray (left panel) and X-ray sources (right panel). Upper limits correspond to galaxies fainter than 11 μJy (3σ limiting flux density) in the 24 μm image. The color tracks for the CWW E/S0 and HR 10 SEDs at $1.5 < z < 3$ are shown in red and blue lines. The blue and red filled circle indicate the locus of their colors at $z = 1.5$ and $z = 3$, respectively. The [3.6] - [24] color provides an estimate of SSFR while the $K-[3.6]$ color is sensitive to dust extinction. The [3.6] – [24] color distribution is clearly bimodal. All the 24 μm-undetected IEROs are at [3.6] – [24] < 0.3, most of which also have bluer $K-[3.6]$ colors. We propose a preliminary color criteria of [3.6] – [24] = 0.3 and $K-[3.6] = 1.2$ to separate quiescent and star-forming galaxies. The central AGN can also have significant contribution to their 24 μm emission, and thus this criterion may not apply to some X-ray IEROs.

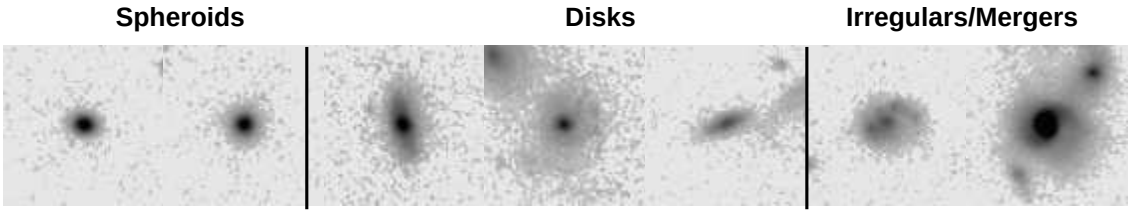

Fig. 3.— For the visual classifications, we simply divide the sample into three broad morphological types: spheroid on the left, disk morphologies in the middle, and irregular/mergers on the right panel.

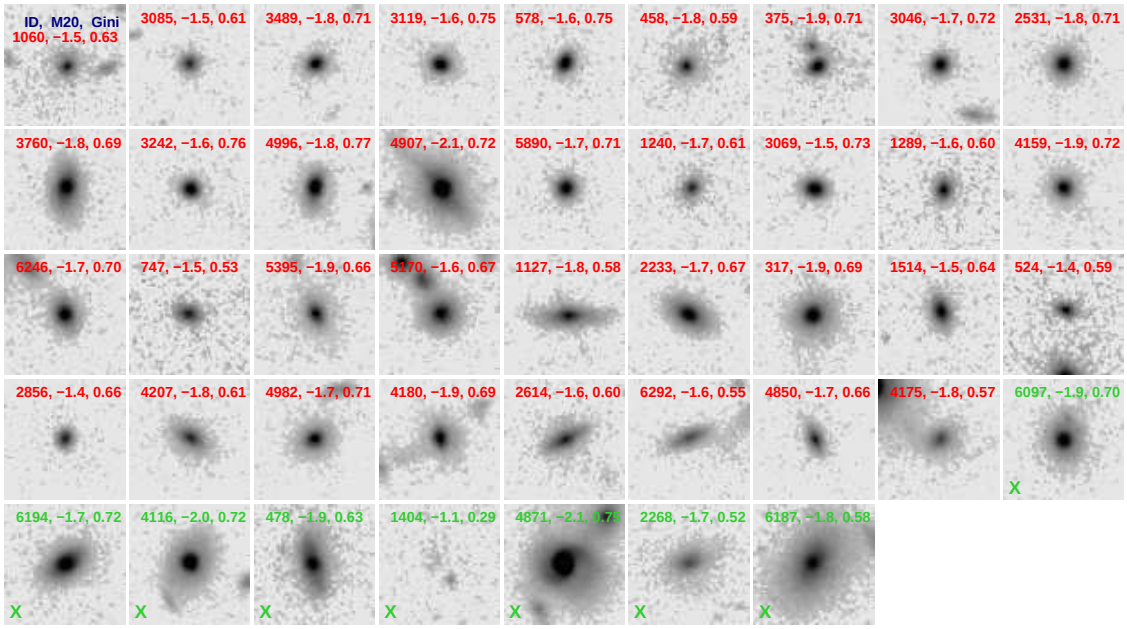

Fig. 4.— *HST*/WFC3 F160W images for the quiescent galaxies (quiescents) in our sample. Quiescents are defined by Eq 1 and lie within the dashed square in Figure 2. The source IDs (from FIREWORKS catalog), M_{20}, and Gini are labeled in each panel. X-ray sources are marked with an "X" in the bottom-left corner. Both non-X-ray and X-ray sources are sorted in order of increasing $K-[3.6]$ colors. The size of each postage map is $4'' \times 4''$, and $1''$ corresponds to ~ 8.5 kpc at $z \sim 2$. Nearly all objects have a prominent bulge component with $\sim 30\%$ of them also showing an extended disk. The only outlier is Object 1404, which shows a very diffuse morphology with a photometric redshift $z \sim 3$. At this redshift, the MIPS 24 μm probes the rest-frame 6 μm, and even star-forming galaxies has low brightness. We thus argue Object 1404 is not a $z \sim 2$ quiescent galaxy.

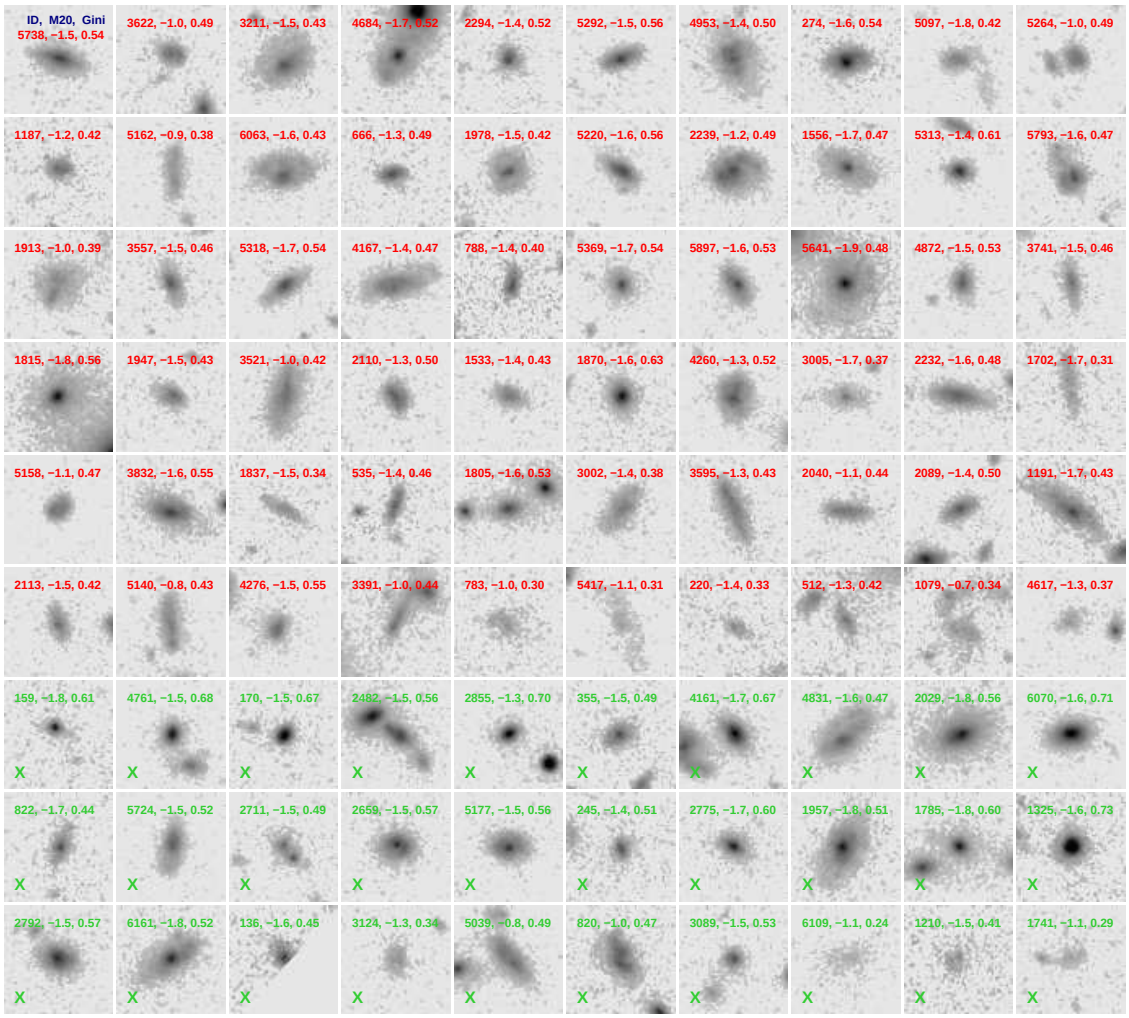

Fig. 5.— *HST*/WFC3 F160W images for the dusty star-forming galaxies (dSFGs) in our sample. The dSFGs are all galaxies that lie outside the dashed square in Figure 2. X-ray sources are marked with green "X". Fireworks ID, M_{20}, and Gini are shown in each postage stamp. Both non-X-ray and X-ray sources are sorted in order of increasing $K-[3.6]$ colors. Most of these dSFGs have disk or irregular/merger morphologies, with only a few of them, mainly X-ray sources, showing a strong bulge component.

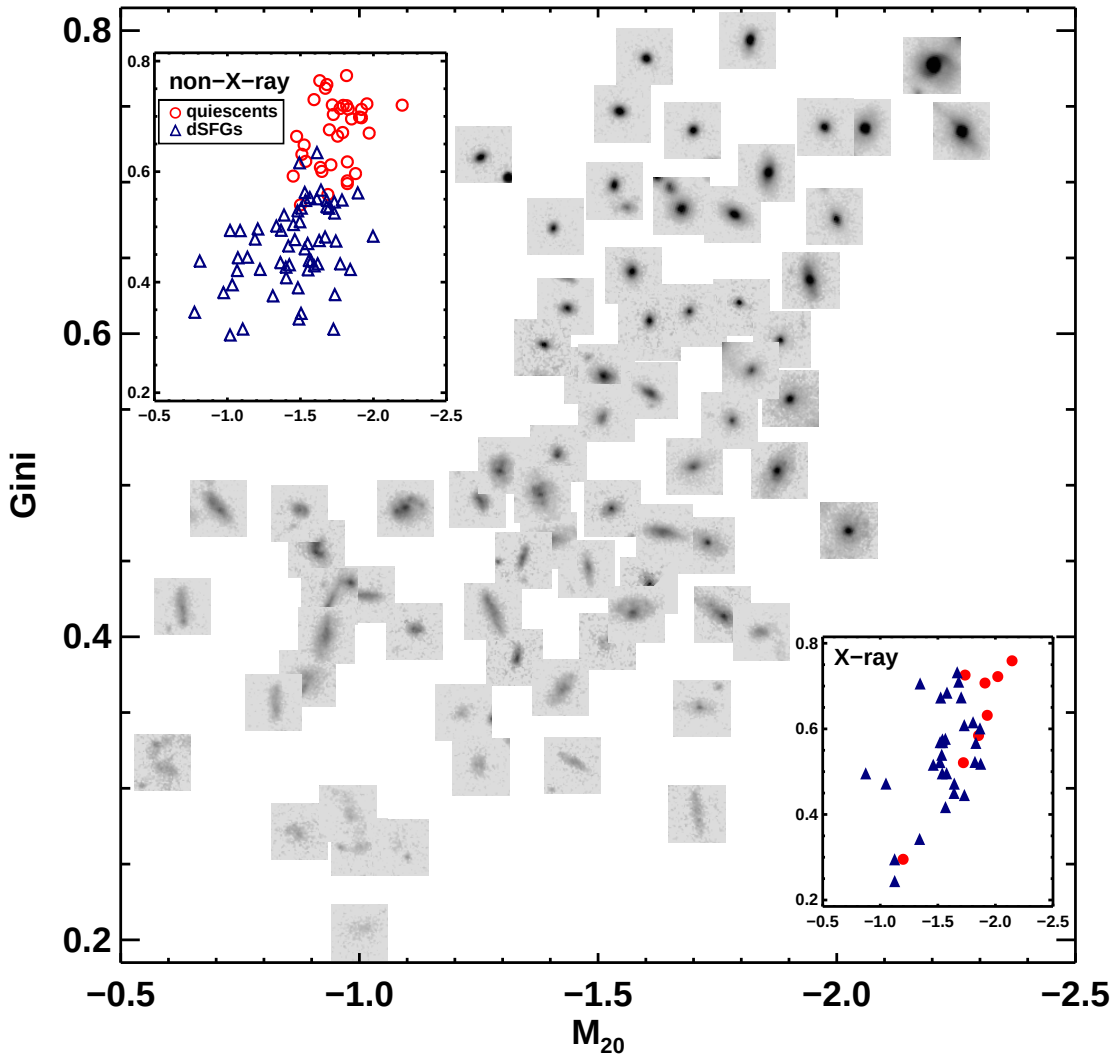

Fig. 6.— Gini vs M_{20} for the galaxies in our sample. Quiescents and dSFGs are defined based on Eq 2. Non-X-ray sources are denoted with circles and triangles while X-ray sources are denoted with filled circles and triangles, respectively. The quiescent and dSFGs are well separated in this diagram (upper left insert). The postage-stamp images for a randomly selected subsample represent morphologies for galaxies in various location of this diagram. The quiescents have high Gini and low M_{20}, and the dSFGs primarily have low Gini but cover a wide range of M_{20}. The quiescent and dusty star forming galaxies with no X-ray detection are well separated by Gini = 0.58 with only a few outliers. The X-ray sources do not show such consistent classifications between morphologies and their IR colors.

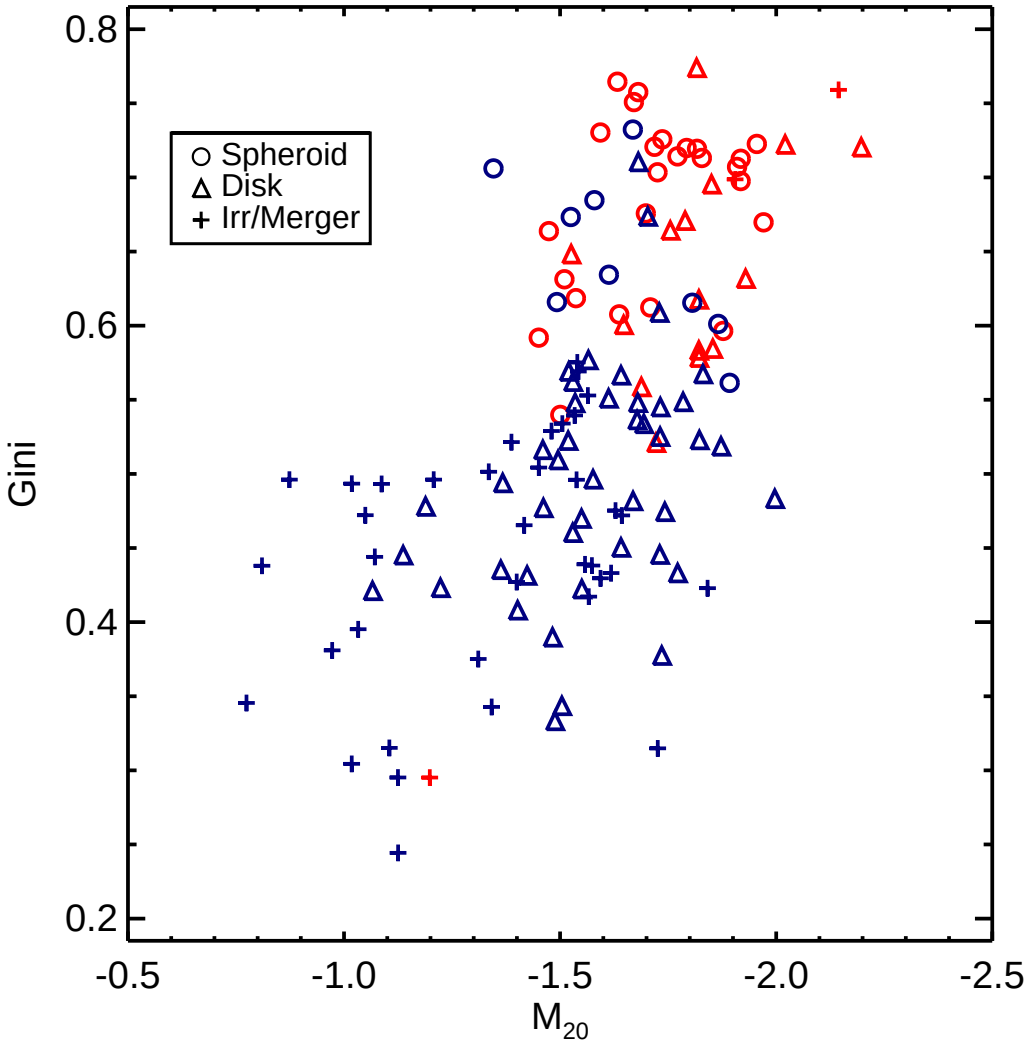

Fig. 7.— The distribution of all the IEROs with different visual morphological types in the *Gini* – M_{20} diagram. Quiescents are denoted with red colors while dSFGs are in blue colors. Their distribution shows great agreement with the visual classification results. Spheroids have higher *Gini* and lower M_{20} while Irr/Mergers have lower *Gini* and higher M_{20}. Interestingly, quiescent disks show primarily higher *Gini* than the star-forming disks, consistent with that the former have a prominent bulge.

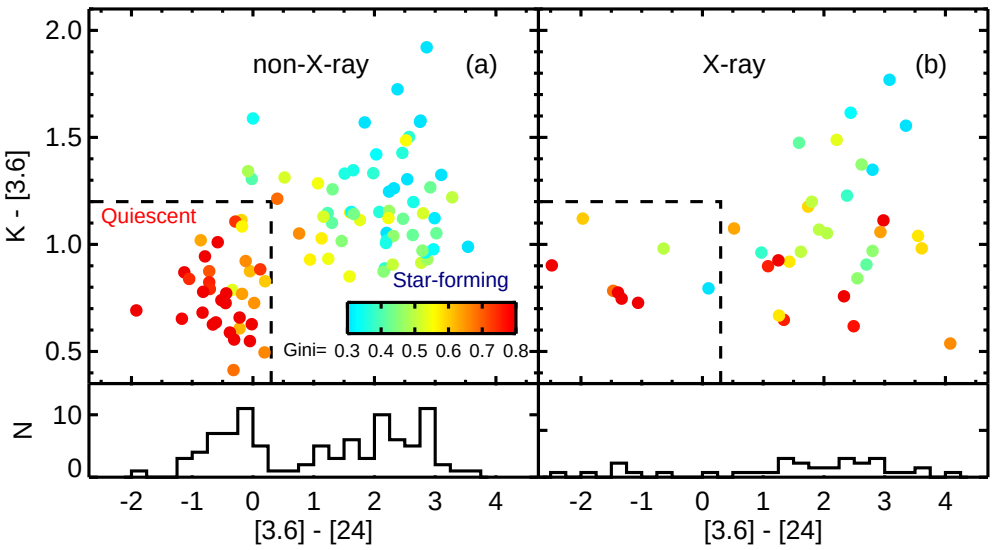

Fig. 8.— [3.6] – [24] vs $K-[3.6]$ color-color diagram for the IERO sample with galaxies color-coded according to the Gini coefficient. A nearly perfect correlation exists between [3.6] – [24] color and Gini. Such a correlation, does not exist for the X-ray sources in the right panel.

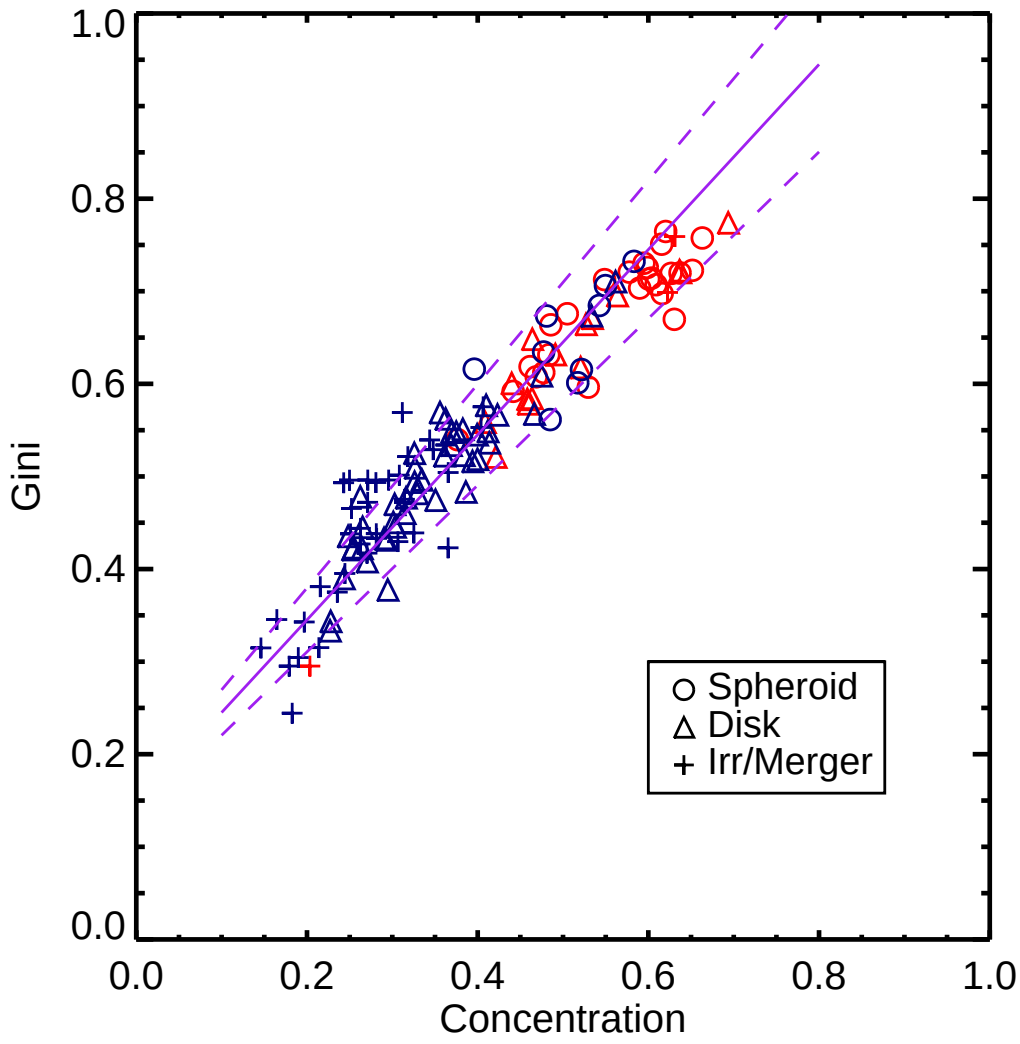

Fig. 9.— Gini coefficient (Gini) vs. central concentration (C) for IEROs in our sample (points as in Figure 7). The solid line corresponds to unity slope, while the dashed lines are ± 10% offset relative to the solid line.

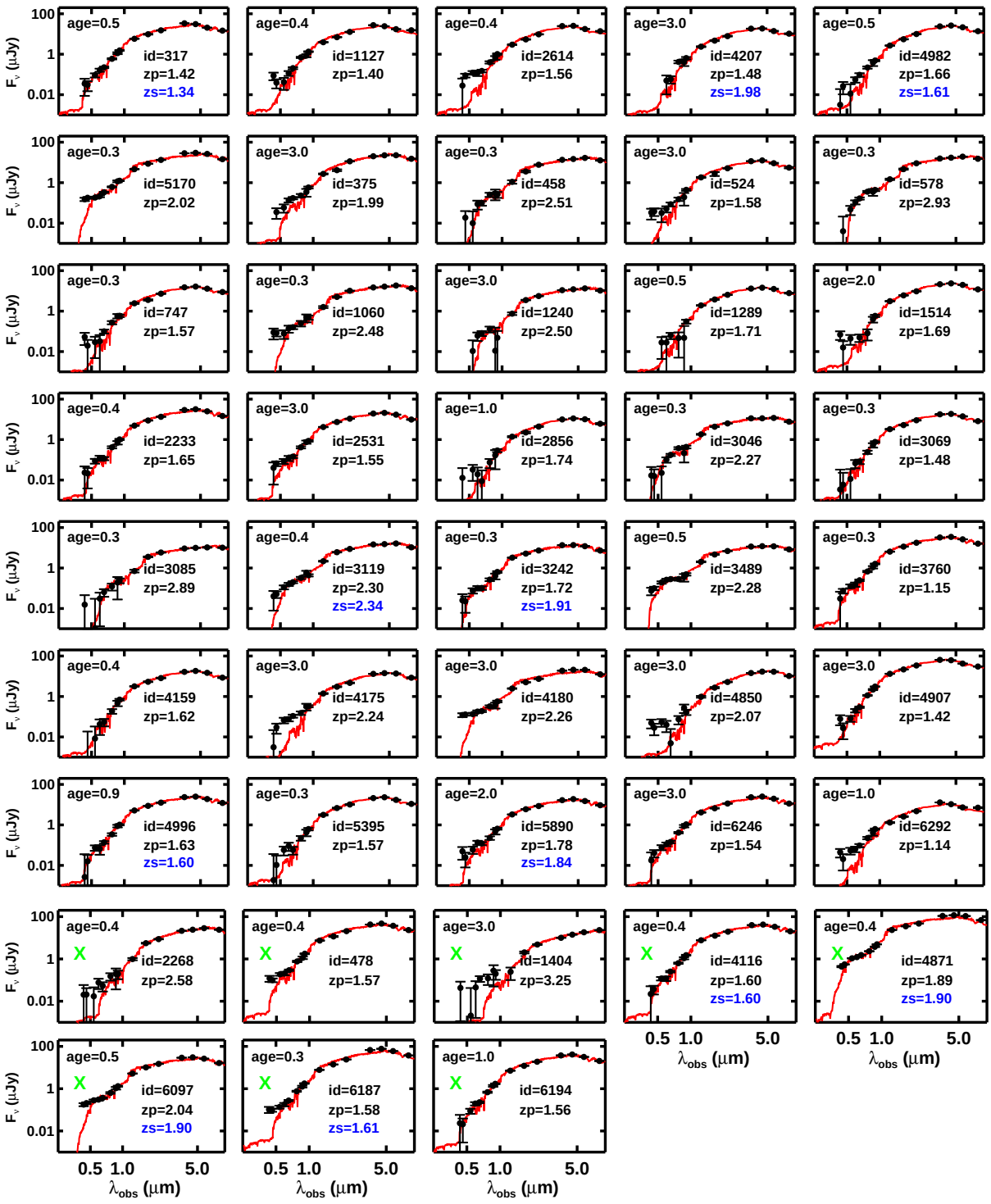

Fig. 10.— SED fitting to measure photometric redshifts for the quiescents with SSP models as templates. The source ID, age of the best-fit SSP model , photometric redshift (z_{ph}) and spectroscopic redshifts(z_{spec}, if available) are labeled in each panel. Most of these quiescents can be well fit with SSP model templates with ages ranging from 0.4 Gyr to the age of the Universe of 4 Gyr at that redshift. "X"s denote the X-ray sources in Figure 4.

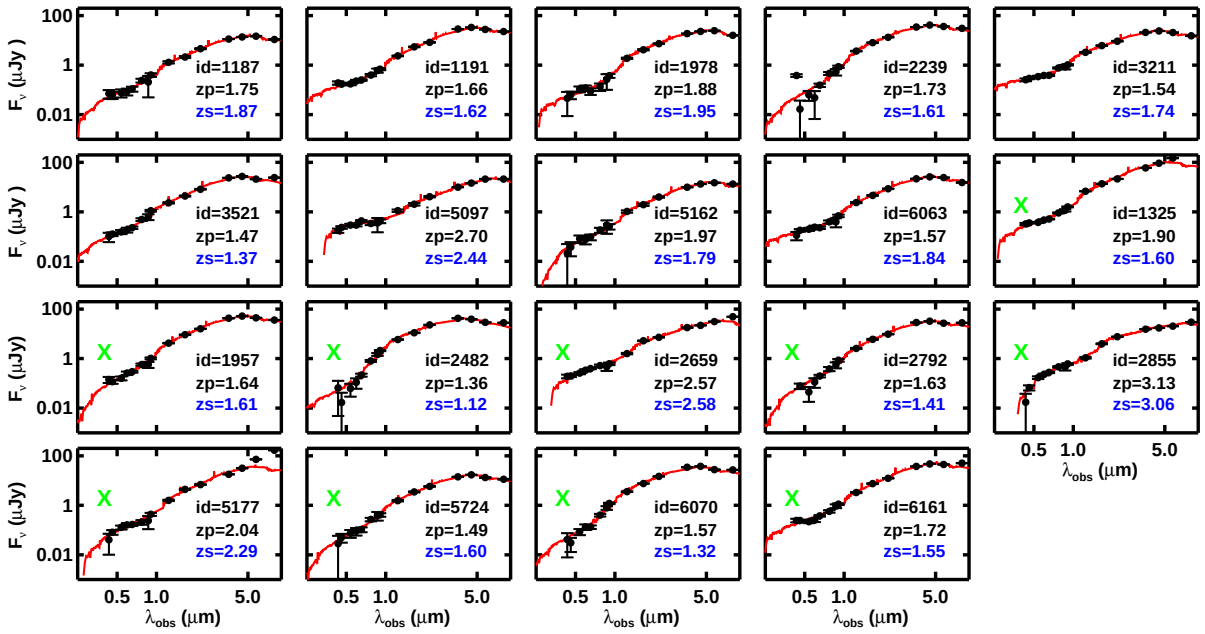

Fig. 11.— Example SEDs for the dSFGs with EAzY spectral fits overlaid. Here we only show the SEDs for those dSFGs with spectroscopic redshifts. Data points with 1σ errors are shown in black. The red line shows the linear combination of template SEDs that best fit the data. The source ID, z_{ph} and z_{spec} are labeled in each panel.

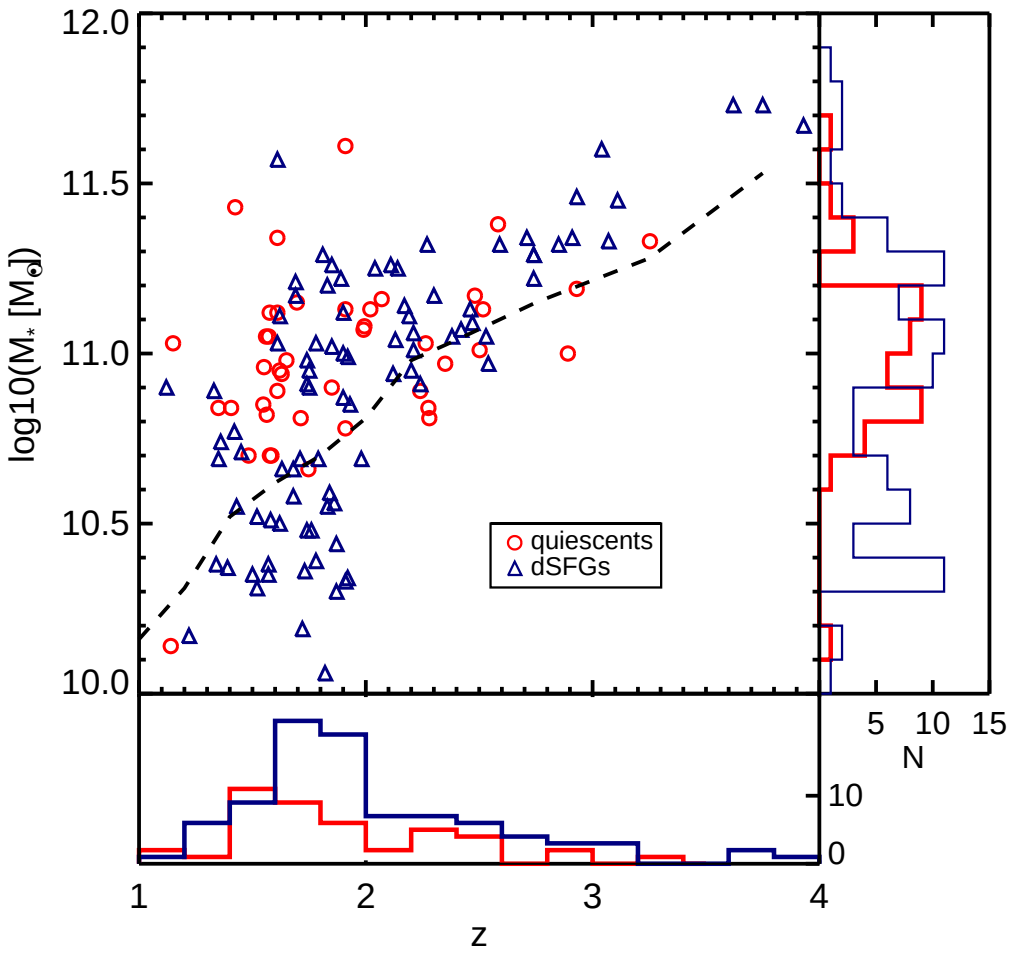

Fig. 12.— Redshift and stellar mass histograms of the full sample. The dashed line corresponds to the mass completeness limit for a 3.6 μm selected sample ([3.6] < 21.5) at $1 < z < 4$. The redshift range of the IERO sample spans from 1 to 4 with most of them located at $1.5 < z < 2.5$, indicating that the simple color criterion of $z_{850} - [3.6] > 3.25$ can effectively select massive galaxies at $z \sim 2$.

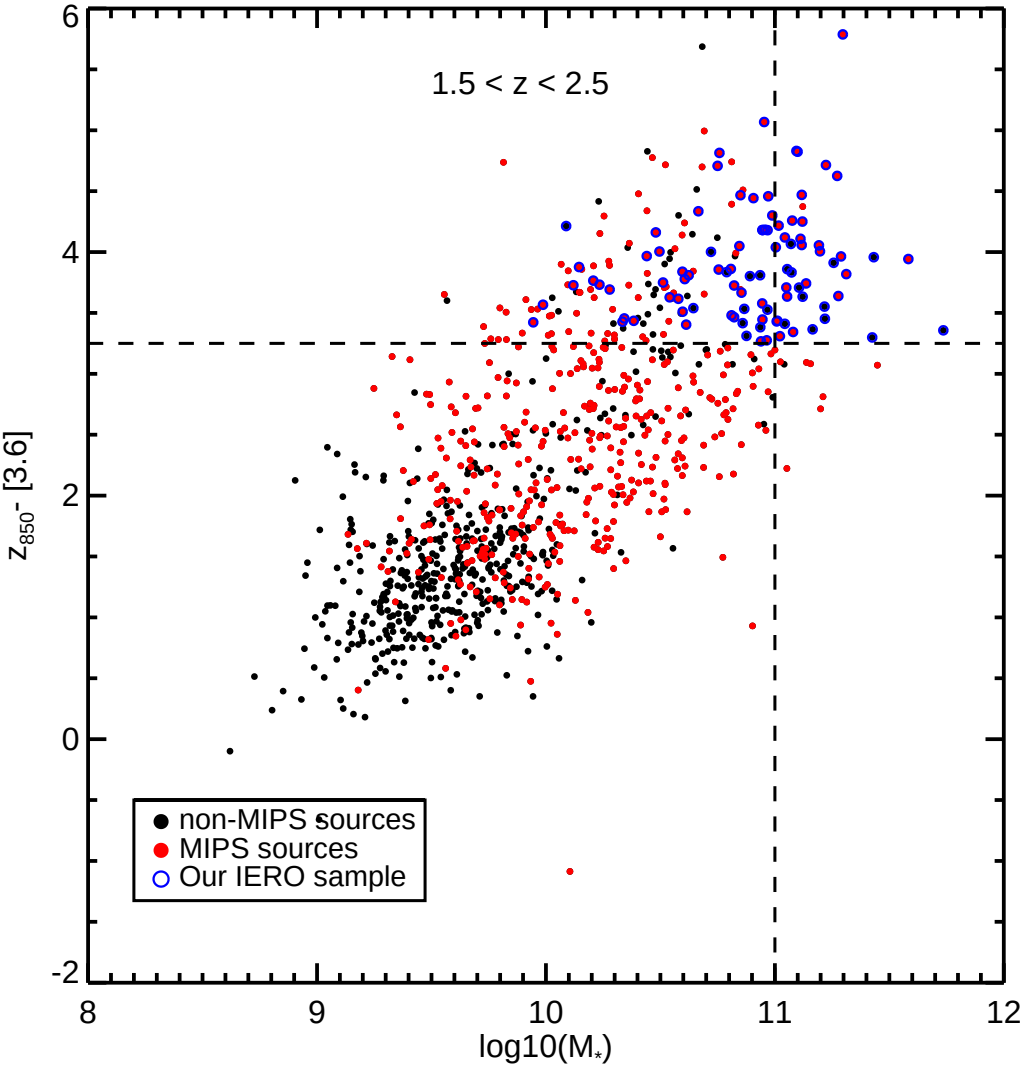

Fig. 13.— $z_{850}-[3.6]$ vs stellar mass for all galaxies at $1.5 < z < 2.5$ in the FIREWORKS catalog. Red points are MIPS sources. The purple open squares are IEROs in our sample ($z_{850}-[3.6] > 3.25$ and $[3.6] < 21.5$). There are 49 galaxies with $M_* > 1 \times 10^{11} M_\odot$, which all have $[3.6] < 21.5$. About 80% of them (39) are selected as IEROs with $z_{850}-[3.6] > 3.25$. Among the nine galaxies not selected as IEROs, four of them are X-ray sources (Luo et al. 2008; Xue et al. 2011), which also have the highest MIPS 24 μm flux and bluest $z_{850}-[3.6]$ colors: $z_{850}-[3.6] < 3.1$. Their SEDs have strong AGN components which may cause their stellar mass to be overestimated. The remaining five galaxies just missed being IEROs according to $z_{850}-[3.6]$ being too blue. Only one of them is not detected at 24 μm.

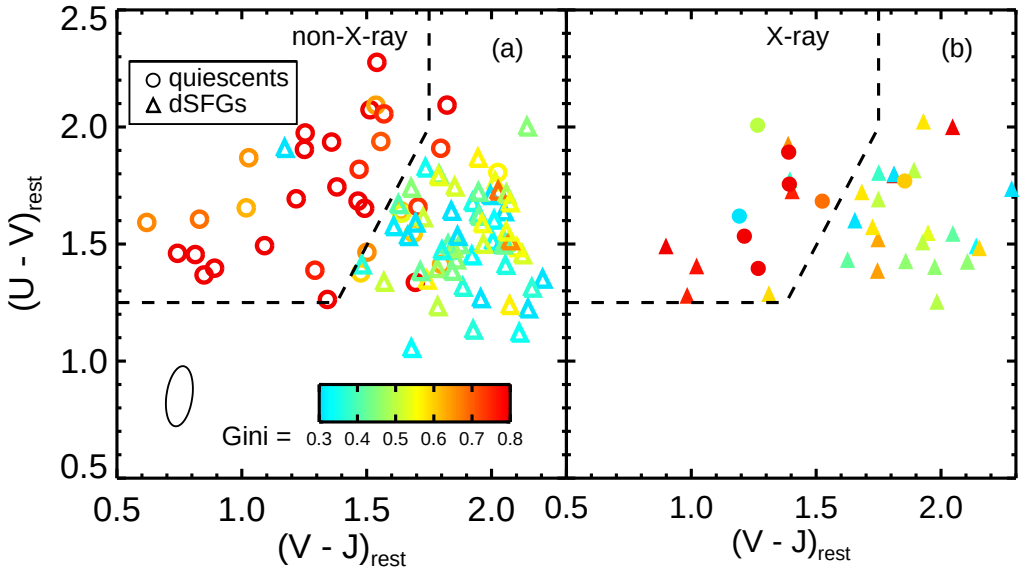

Fig. 14.— Rest-frame $U-V$ vs. $V-J$ color-color diagram for non-X-ray (left) and X-ray (right) IEROs in our sample. The error ellipse is shown in the lower left of the left papel. Objects are color-coded based on Gini coefficient. Quiescent and dSFGs can be well separated in this diagram with the dashed line. The locations of high- vs. low-Gini objects on opposite side to the lines confirms that morphology and rest-frame color-color yield generally consistent classifications for both populations. The distributions overlap somewhat, but mostly near the boundary. Both massive quiescent and dusty galaxies have red $U-V$ colors, but the quiescents are bluer in $V-J$, implying they are not suffering significant dust extinction. X-ray sources with different Gini values are about as well separated as non-X-ray sources (right panel).

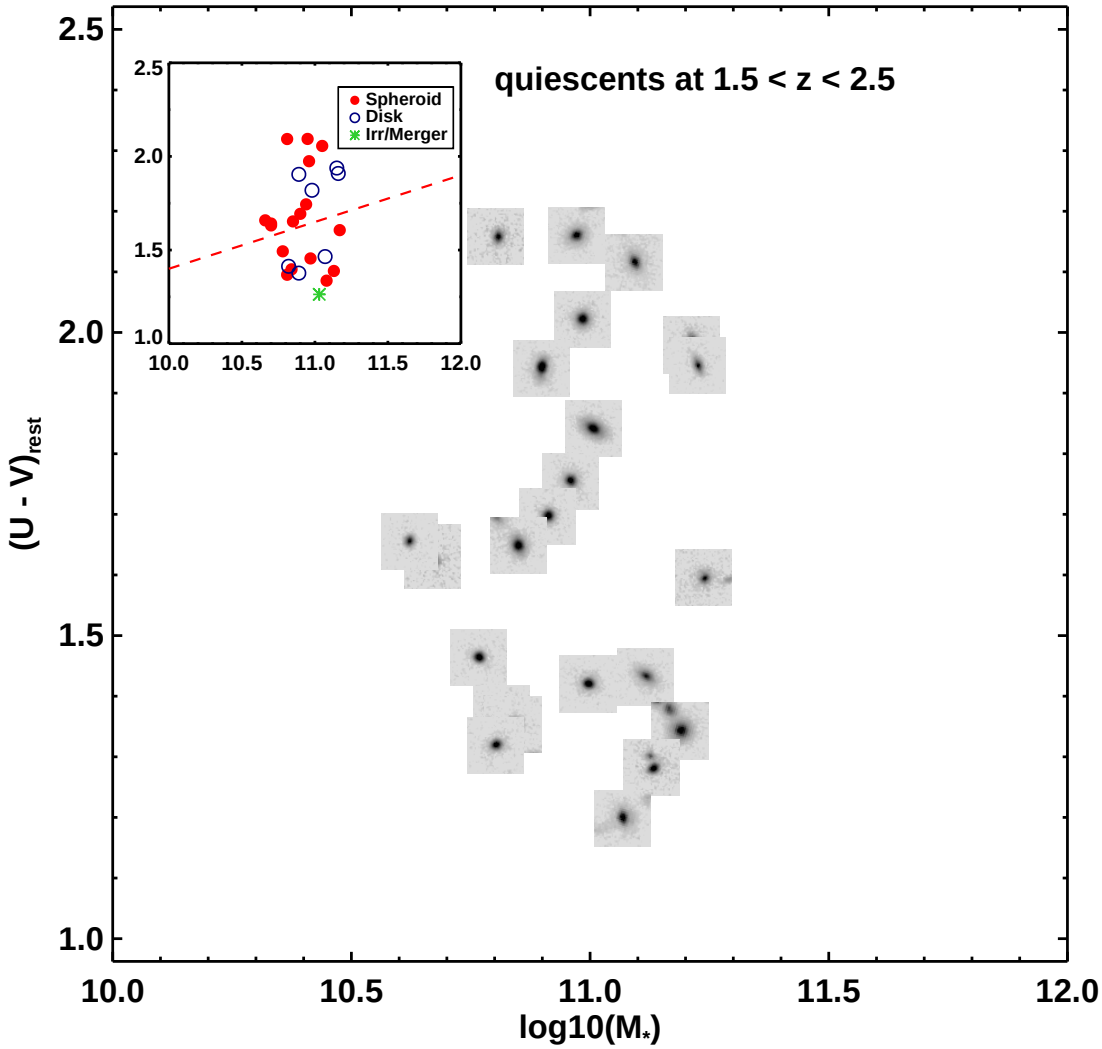

Fig. 15.— Rest-frame $U-V$ color vs stellar mass for quiescents in $1.5 < z < 2.5$ in the sample. *HST*/WFC3 F160W images are also shown. Visual classification results for these quiescents are shown in the upper left panel. The dashed red line is the red sequence criterion at $z = 2$ extrapolated from the same criterion at $z < 1$ in Borch et al. (2006).

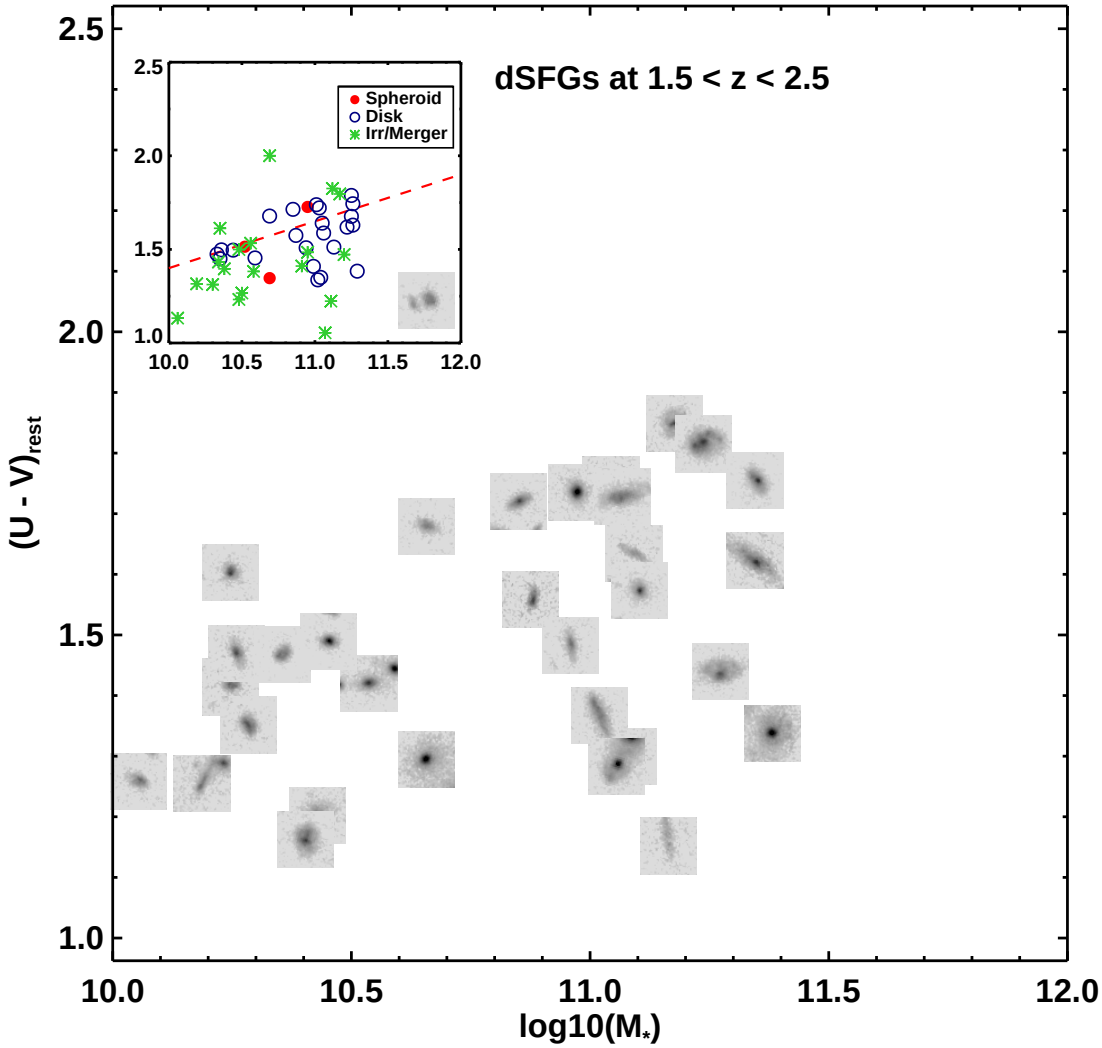

Fig. 16.— Rest-frame $U-V$ color vs stellar mass for dSFGs at in $1.5 < z < 2.5$ in the sample, also shown are *HST*/WFC3 F160W images for a randomly selected dSFGs sample. Visual classification results for the dSFGs are shown in the upper left panel. Most of the dSFGs with $M_* > 1 \times 10^{11} M_\odot$ show disk morphologies.